

Sensing with submarine optical cables

Antonio Mecozzi¹

Department of Physical and Chemical Sciences, University of L'Aquila, L'Aquila, Italy

(*Electronic mail: antonio.mecozzi@univaq.it)

(Dated: 25 April 2024)

In this paper, we establish the theoretical framework for understanding the sensing capabilities of optical fibers. We show the distinct advantage of polarization over phase in detecting subhertz environmental processes. Subsequently, we propose a scheme capable of extracting the spectrum of perturbations affecting a specific section at any position along an optical fiber by detecting the state of polarization of the backreflected light. We discuss two examples of earthquake detection and the detection of sea swells and ocean tides through the analysis of the state of polarization of an optical signal reconstructed by the receiver of a transoceanic cable, obtained from an online database.¹ Finally, we provide the analytical expression for the cross-correlation of the polarization perturbations of two wavelength division multiplexed channels, and show that the analysis of the polarization correlations between adjacent channels can provide valuable insights into the localization of earthquakes.

I. INTRODUCTION

Fiber sensing technologies have emerged as powerful tools for environmental monitoring, enabling precise and real-time data collection over large geographical areas. Taking advantage of the inherent properties of optical fibers, such as low loss transmission and sensitivity to external perturbations, researchers have developed innovative techniques to detect various environmental parameters, including seismic activity, ocean dynamics, and submarine fault detection. Marra et al. introduced ultrastable laser interferometry for earthquake detection using terrestrial and submarine cables,² paving the way towards exciting progress towards disaster management and early warning systems. In ref. 3 and 4 the authors demonstrated the use of optical coherent detection for environmental sensing, showing the potential of polarization sensing in applications such as earthquake detection and tsunami warning. In addition to seismic monitoring, fiber sensing technologies have been applied to understand ocean dynamics and detect underwater phenomena. Lindsey et al.⁵ demonstrated the use of dark fiber distributed acoustic sensing for mapping seafloor faults and monitoring ocean dynamics, while Landrø et al.⁶ utilized arctic fiber optic cables for sensing whales, storms, ships, and earthquakes, proving the versatility of fiber sensing in harsh environments. Skarvang et al.⁷ presented observations of local small magnitude earthquakes using state-of-polarization monitoring in a passive arctic submarine communication cable, highlighting the potential of polarization-based sensing techniques in seismic monitoring. These developments underscore the importance of fiber sensing in enhancing our understanding of environmental processes and facilitating early detection of natural hazards. Using the capabilities of optical fibers, researchers continue to push the boundaries of environmental sensing, enabling more efficient and reliable monitoring of the planet.

In this paper, we will first establish the theoretical basis for the understanding of the sensing capability of optical fibers. We will show the pros and cons of the use of the polarization-averaged optical phase and of the polarization as a sensing tool. We will propose a scheme that can provide the spectrum of the perturbation acting upon the cable by detecting the state

of polarization of the backreflected light. We will then delve into the vast database in ref. 1 to show a few examples of earthquake detection using the reconstructed state of polarization of the receiver of the Curie cable system connecting Los Angeles, in California, to Valparaiso in Chile. Finally, we will present an analytical expression of the cross-correlation of the state of polarization between two wavelength division multiplexed channels and highlight how studying the correlations between the polarization of nearby channels may yield valuable insights into localization of earthquakes.

II. BASIC EQUATIONS

Let the tranverse electric field propagating in a single mode fiber be represented by the column vector

$$\begin{bmatrix} \mathcal{E}_x(z) \\ \mathcal{E}_y(z) \end{bmatrix} = \begin{bmatrix} E_x(z) \\ E_y(z) \end{bmatrix} \exp(-i\omega_0 t), \quad (1)$$

where ω_0 is the center optical frequency. Let us define

$$\begin{bmatrix} E_x(z) \\ E_y(z) \end{bmatrix} = A(z) |\vec{s}(z)\rangle, \quad (2)$$

where $A(z) = [|E_x(z)|^2 + |E_y(z)|^2]^{1/2}$ and

$$|\vec{s}(z)\rangle = \begin{bmatrix} s_x(z) \\ s_y(z) \end{bmatrix}, \quad (3)$$

is a Jones vector, normalized such that

$$\langle \vec{s}(z) | \vec{s}(z) \rangle = 1. \quad (4)$$

Here, following Dirac's bra-ket notation, we defined $\langle \vec{s}(z) | = (|\vec{s}(z)\rangle)^\dagger$, with the dagger standing for hermitian conjugation (the transpose conjugate of the vector). Assuming negligible polarization dependent loss and gain, the evolution of the amplitude of the field $A(z)$ is only determined by the gain and loss profile of the fiber, and decouples to that of the polarization. In a right-handed reference frame with x and y in the transverse

plane and z in the propagation direction, the propagation of the Jones vector can then be described by the equation

$$\frac{d}{dz}|\vec{s}(z)\rangle = i\mathbf{V}(z)\mathbf{B}(z)\mathbf{V}^\dagger(z)|\vec{s}(z)\rangle, \quad (5)$$

where $\mathbf{V}(z)$ is the unitary matrix

$$\mathbf{V}(z) = \begin{bmatrix} \cos\theta(z) & -\sin\theta(z) \\ \sin\theta(z) & \cos\theta(z) \end{bmatrix} \quad (6)$$

representing an anticlockwise rotation by the angle $\theta(z)$ of in the $x-y$ plane with respect to the z axis, so that $\mathbf{V}(z)\mathbf{B}(z)\mathbf{V}^\dagger(z)$ produces a rotation by the same angle of the birefringence vector, and

$$\mathbf{B}(z) = \begin{bmatrix} \beta_1(z) & 0 \\ 0 & \beta_2(z) \end{bmatrix}, \quad (7)$$

with $\beta_1(z)$ and $\beta_2(z)$ the magnitudes of the (local) eigenvalues of the transmission matrix. Defining the Pauli matrices as

$$\sigma_1 = \begin{pmatrix} 1 & 0 \\ 0 & -1 \end{pmatrix}, \quad \sigma_2 = \begin{pmatrix} 0 & 1 \\ 1 & 0 \end{pmatrix}, \quad \sigma_3 = \begin{pmatrix} 0 & i \\ -i & 0 \end{pmatrix}, \quad (8)$$

and the Pauli spin vector as the Stokes vector $\vec{\sigma} = \sigma_1\hat{e}_1 + \sigma_2\hat{e}_2 + \sigma_3\hat{e}_3$, where \hat{e}_i are the canonical basis vectors of Stokes space, Eq. (5) becomes

$$\frac{d}{dz}|\vec{s}(z)\rangle = i \left[\beta_0(z)\mathbb{1} + \frac{\vec{\beta}(z)}{2} \cdot \vec{\sigma} \right] |\vec{s}(z)\rangle, \quad (9)$$

where $\mathbb{1}$ is the two-by-two unit matrix, and

$$\beta_0(z) = \frac{1}{2} [\beta_1(z) + \beta_2(z)], \quad (10)$$

$$\vec{\beta}(z) = \beta(z) \cos[2\theta(z)]\hat{e}_1 + \beta(z) \sin[2\theta(z)]\hat{e}_2, \quad (11)$$

with

$$\beta(z) = \beta_1(z) - \beta_2(z). \quad (12)$$

Solution of Eq. (5) is

$$|\vec{s}(z)\rangle = \mathbf{U}_0(z)|\vec{s}(0)\rangle, \quad (13)$$

where $\mathbf{U}_0(z)$ satisfy the equation

$$\frac{d\mathbf{U}_0(z)}{dz} = i \left[\beta_0(z)\mathbb{1} + \frac{\vec{\beta}(z)}{2} \cdot \vec{\sigma} \right] \mathbf{U}_0(z), \quad (14)$$

with initial condition $\mathbf{U}_0(0) = \mathbb{1}$. Using in Eq. (14) the expansion

$$\mathbf{U}_0(z) = \exp[i\varphi_0(z)]\mathbf{U}(z), \quad (15)$$

we obtain the equation

$$i\frac{d\varphi_0(z)}{dz}\mathbf{U}(z) + \frac{d\mathbf{U}(z)}{dz} = i \left[\beta_0(z)\mathbb{1} + \frac{\vec{\beta}(z)}{2} \cdot \vec{\sigma} \right] \mathbf{U}(z), \quad (16)$$

which is verified if

$$\frac{d\varphi_0(z)}{dz} = \beta_0(z), \quad (17)$$

and

$$\frac{d\mathbf{U}(z)}{dz} = \frac{i}{2} [\vec{\beta}(z) \cdot \vec{\sigma}] \mathbf{U}(z), \quad (18)$$

with initial conditions $\varphi_0(0) = 0$ and $\mathbf{U}(0) = \mathbb{1}$. The solution of Eq. (18) can be formally written as

$$\mathbf{U}(z) = \prod_{z'=0}^z \exp \left[\frac{i}{2} \vec{\beta}(z') \cdot \vec{\sigma} dz' \right], \quad (19)$$

with the individual members of the product belonging to $SU(2)$ (the special unitary group of degree 2, which is the group of unitary two-by-two matrices of unit determinant). Being $SU(2)$ closed with respect to matrix multiplication,⁸ $\mathbf{U}(z)$ itself is a member of $SU(2)$.^{9,10} Defining the polarization averaged phase as

$$\bar{\varphi}_0 = \frac{1}{2i} \text{trace} \log \mathbf{U}_0 = \frac{1}{2i} \log \det \mathbf{U}_0, \quad (20)$$

it is easy to show, using Eq. (15) and the property that $\mathbf{U}(z)$ belongs to $SU(2)$ hence its determinant is one, that

$$\bar{\varphi}_0 = \varphi_0 + \frac{1}{2i} \log \det \mathbf{U} = \varphi_0. \quad (21)$$

so that the polarization averaged phase is the solution of Eq. (17). A member of the $SU(2)$ group can always be expressed as^{9,10}

$$\mathbf{U}(z) = \exp \left[\frac{i}{2} \vec{\varphi}(z) \cdot \vec{\sigma} \right], \quad (22)$$

so that

$$\mathbf{U}_0(z) = \exp \left[i\varphi_0(z)\mathbb{1} + \frac{i}{2} \vec{\varphi}(z) \cdot \vec{\sigma} \right]. \quad (23)$$

Being $\varphi_0(z)$ solution of Eq. (17), it is not affected by the rotation of the birefringence axes. Consequently, the fluctuations of the average phase are insensitive to the rotation of the birefringence axes, or equivalently, they are uncoupled to the fluctuations that leave unchanged the modulus of the birefringence eigenvalues. Consequence of this property is that, as we will see, fiber twist does not affect the polarization averaged phase. The evolution of the phase fluctuations can be expressed in terms of the polarization averaged wavevector by simply integrating Eq. (17)

$$\varphi_0(z) = \int_0^z \beta_0(z') dz'. \quad (24)$$

Let us define the Stokes vector corresponding to $|\vec{s}(z)\rangle$ as⁹

$$\vec{s}(z) = \langle \vec{s}(z) | \vec{\sigma} | \vec{s}(z) \rangle. \quad (25)$$

This vector describes in Stokes space the evolution of the field polarization. The equation describing the evolution of $\vec{s}(z)$ can be obtained using Eq. (13) in the definition of Stokes vector

$$\vec{s}(z) = \langle \vec{s}(0) | \mathbf{U}^\dagger(z) \vec{\sigma} \mathbf{U}(z) | \vec{s}(0) \rangle \quad (26)$$

differentiating both terms and using Eq. (18) and the equality $(\vec{a} \cdot \vec{\sigma})\vec{\sigma} = \vec{a}\mathbf{1} + i\vec{a} \times \vec{\sigma}$ and that $\vec{\sigma}(\vec{a} \cdot \vec{\sigma}) = \vec{a}\mathbf{1} - i\vec{a} \times \vec{\sigma}$. The final result is⁹

$$\frac{d\vec{s}(z)}{dz} = \vec{\beta}(z) \times \vec{s}(z). \quad (27)$$

Having derived the fundamental equations, the following section will be devoted to the analysis of the effect of external perturbations on the polarization averaged wavevector β_0 and on the fiber birefringence $\vec{\beta}$.

III. WAVEVECTOR PERTURBATIONS

Let us consider a perfectly cylindrical fiber and treat any effects of the deviations from cylindrical symmetry (including birefringence) as a small perturbation. Assume first a perfectly cylindrical fiber with no preexisting birefringence. If some strain is applied to the fiber, the polarization averaged wavevector $\beta_0 = 2\pi n_0/\lambda$ turns into

$$\beta_0 = \frac{2\pi}{\lambda} n(z), \quad (28)$$

where $n(z)$ is the refractive index given by

$$n(z) = n_0 + C\varepsilon(z). \quad (29)$$

Here, n_0 is the unperturbed glass refractive index, C is the photoelastic factor and $\varepsilon(z)$ the strain. The strain also affects the propagation distance at every z , becoming $z(\varepsilon) = [1 + \varepsilon(z)]z$. Thus, dz turns into $dz'(\varepsilon) = [1 + \varepsilon(z')]dz'$ and φ_0 changes to

$$\varphi(z) = \int_0^z \frac{2\pi}{\lambda} [n_0 + C\varepsilon(z')] [1 + \varepsilon(z')] dz'. \quad (30)$$

Neglecting the term of the order of ε^2 we obtain

$$\varphi(z) = \beta_0 \int_0^z [1 + \xi \varepsilon(z')] dz'. \quad (31)$$

where $\xi = 1 + C/n_0$ is the photoelastic scaling factor for longitudinal strain (for isotropic glass, $\xi \simeq 0.78$), and

$$\beta_0 = \frac{2\pi}{\lambda} n_0 \quad (32)$$

is the unperturbed wavevector. The effect of strain is to produce to the polarization averaged propagation constant the relative change

$$\frac{\Delta\beta}{\beta_0} = \xi \varepsilon. \quad (33)$$

Assume now that the fiber has some (small) birefringence and treat the effects of the birefringence as a perturbation.

If the strain is induced by hydrostatic pressure via the Poisson effect, the cylindrical symmetry of the perturbation implies that it does not alter the orientation of the birefringence vector, meaning that $\Delta\vec{\beta}$ is parallel to $\vec{\beta}$. Moreover, a perturbation with cylindrical symmetry cannot induce birefringence in a cylindrical fiber, since any nonzero birefringence would break the cylindrical symmetry. This requirement is satisfied if we assume that the perturbation alters the eigenvector on each eigenpolarization proportionally to the magnitude of the wavevector itself. Enforcing this condition alongside the additional criterion that Eq. (33) is recovered when birefringence is absent results in

$$\frac{\Delta\beta_h}{\beta_h} = \xi \varepsilon \quad h = 1, 2. \quad (34)$$

The use of this equation for $h = 1$ and 2 gives

$$\frac{\Delta\beta_1 - \Delta\beta_2}{\beta_1 - \beta_2} = \xi \varepsilon, \quad (35)$$

that is, being $\Delta\beta_1(z) - \Delta\beta_2(z) = \Delta\beta$ and $\beta_1 - \beta_2 = \beta$, the equation $\Delta\beta = \xi \varepsilon \beta$. The additional condition of parallelism between $\Delta\vec{\beta}$ and $\vec{\beta}$ yields the expression

$$\Delta\vec{\beta} = \xi \varepsilon \vec{\beta}. \quad (36)$$

We obtain the important result that in quasi-cylindrical symmetric fibers, in which birefringence is a small perturbation, the dependence of the birefringence on strain can be inferred from the dependence on strain of the polarization averaged wavevector, which is easier to characterize experimentally.⁴

Another process affecting birefringence is the twist of the fiber. We have shown in the previous section that the fluctuations of the average phase are insensitive to rotations of the birefringence axes that leave unchanged the modulus of the birefringence eigenvalues, so that fiber twist, unlike strain, does not modify the polarization-averaged wavevector and phase. When the fiber is twisted by an angle α around its axis, the first-order change in birefringence is given by

$$\Delta\vec{\beta} = 2\alpha \hat{e}_3 \times \vec{\beta}. \quad (37)$$

Notice that \hat{e}_3 and $\vec{\beta}$ are orthogonal so that $\Delta\vec{\beta}$ belongs to the (\hat{e}_1, \hat{e}_2) plane of Stokes space and $\Delta\beta = 2|\alpha|\beta$.

In both cases of strain and twist, the magnitude of the birefringence perturbation is proportional to the pre-existing static birefringence. This characteristic enables the establishment of a correlation between a fiber's sensitivity to external perturbations and the fiber's polarization mode dispersion, a correlation we will elaborate on in Section V.

IV. PHASE-BASED SENSING

Phase sensing relies on measuring the perturbation to the phase of an optical field propagating along an optical fiber due to strain induced by coupling with the surrounding environment. In the previous section, it was demonstrated that strain

causes a local alteration in the polarization-averaged wavevector, as described by Eq. (33). Consequently, this modification affects the polarization-averaged phase accumulated over a distance z adding to Eq. (24) the term

$$\Delta\varphi(z, t) = \int_0^z \Delta\beta(z', t) dz', \quad (38)$$

which is equal to, using Eq. (33)

$$\Delta\varphi(z, t) = \frac{2\pi}{\lambda} n_0 \int_0^z \xi \varepsilon(z', t) dz'. \quad (39)$$

The primary noise source that limits the sensitivity of phase measurements is the phase noise of the laser probe. In the following, we examine the limitations that phase noise imposes on the sensitivity of phase measurements. Consider a laser with quantum-limited white frequency noise. Accurate detection of the phase deviation occurring over the time T

$$\Delta\varphi_{\text{sig}}(T) = \Delta\varphi(z, t+T) - \Delta\varphi(z, t), \quad (40)$$

requires that $|\Delta\varphi_{\text{sig}}(T)| \gg \Delta\varphi_{\text{rms}}$, where $\Delta\varphi_{\text{rms}}$ is the root-mean square of the phase deviation due to the laser phase noise. The phase fluctuations of a quantum limited laser are described by a Wiener process with diffusion constant $D_\varphi = 2\pi\nu$, where ν is the laser linewidth. After a time T the root-mean square phase deviations originating from the laser phase noise are therefore

$$\Delta\varphi_{\text{rms}}(T) = \langle \Delta\varphi_{\text{sig}}^2(T) \rangle^{1/2} = \sqrt{D_\varphi T}. \quad (41)$$

The condition $|\Delta\varphi_{\text{sig}}(T)| \gg \Delta\varphi_{\text{rms}}$ becomes

$$|\Delta\varphi_{\text{sig}}(T)| \gg \sqrt{D_\varphi T}. \quad (42)$$

If the rate of variation of the phase is $\dot{\varphi}$, then $\Delta\varphi_{\text{sig}}(T) = \dot{\varphi}T$ and Eq. (42), after using the expression for D_φ in terms of the linewidth, becomes

$$|\dot{\varphi}|T \gg \sqrt{2\pi\nu T}, \quad (43)$$

that is

$$\nu \ll \frac{\dot{\varphi}^2 T}{2\pi}. \quad (44)$$

A longer sampling time effectively averages the effects of laser phase noise, thereby reducing the requirements on the linewidth. However, the 2π periodicity of the phase imposes that $|\Delta\varphi_{\text{sig}}| = |\dot{\varphi}|T \leq 2\pi$. Using for T its maximum value $2\pi/|\dot{\varphi}|$, we obtain the somehow expected result

$$\nu \ll |\dot{\varphi}|. \quad (45)$$

This condition was met in the earthquake detection cases presented in ref. 2, wherein the earthquakes induced a phase dynamics covering intervals on the order of thousands of radians over a timescale of tens of seconds, and the laser employed had sub-hertz equivalent linewidth. It is questionable whether the detection of processes with much weaker dynamics that occur over the same timescale or longer, like those associated

with tsunami's propagation, would be possible even utilizing lasers with similar ultra-low linewidth.

Let us now consider a different scenario, namely that the process is characterized by a bandwidth $1/(2T)$ and is recorded for a duration sufficient to utilize the short-time Fourier transform for its analysis.¹¹ Let $\varphi_0(t)$ be the phase corrupted by the laser phase noise. The instantaneous frequency perturbed by the frequency noise of the laser has the expression

$$\frac{d\varphi_0(t)}{dt} = N_0(t) + \frac{d\varphi(t)}{dt}, \quad (46)$$

and where $N_0(t)$ is the frequency noise of a quantum limited laser with linewidth ν , namely a white noise term with correlation function

$$\langle N_0(t)N_0(t') \rangle = D_\varphi \delta(t-t'). \quad (47)$$

Let us assume that the signal spectrum is entirely contained within a bandwidth $1/(2T)$. Complete signal reconstruction can be accomplished by sampling the signal at intervals of T . Let $n \gg 1$ be the number of samples, so that the overall detection window is nT . Optimal signal reconstruction is achieved by convolution of the signal plus noise with the matched filter

$$F(t) = (1/T) \text{sinc}(t/T), \quad (48)$$

where $\text{sinc}(x) = \sin(\pi x)/(\pi x)$. After filtering, Eq. (47) becomes

$$\frac{d\varphi_0(t)}{dt} = N(t) + \frac{d\varphi(t)}{dt}, \quad (49)$$

where

$$N(t) = \int_{-\infty}^{\infty} F(t-t')N_0(t')dt', \quad (50)$$

while the second term at right-hand side of Eq. (49), its spectrum being entirely contained within the filter bandwidth, remains unaltered by filtering. Let us define the spectra

$$\tilde{N}(\Omega_k) = \frac{1}{n} \sum_{h=0}^{n-1} N(hT) \exp(i\Omega_k hT), \quad (51)$$

$$\tilde{\varphi}(\Omega_k) = \frac{1}{n} \sum_{h=0}^{n-1} \varphi(hT) \exp(i\Omega_k hT), \quad (52)$$

and likewise, the spectrum of $\varphi_0(t)$. Here, the angular frequencies have the discrete values (assuming n even)

$$\Omega_k = \frac{2\pi k}{nT}, \quad k = -n/2 + 1, \dots, n/2. \quad (53)$$

We employed a normalization factor $1/n$ in the Fourier transform definition to ensure that the spectral amplitude $\tilde{\varphi}(\Omega_k)$ of a pure sinusoidal modulation at frequency Ω_k is independent of the number of samples n . Fourier transforming both sides of Eq. (49) yields

$$i\Omega_k \tilde{\varphi}_0(\Omega_k) = \tilde{N}(\Omega_k) + i\Omega_k \tilde{\varphi}(\Omega_k). \quad (54)$$

Using Eq. (47) into Eq. (50), we obtain

$$\langle N(hT)N(kT) \rangle = \frac{2\pi\nu}{T} \delta_{h,k}. \quad (55)$$

Taking the square of Eq. (51), averaging and using Eq. (55) yields

$$\langle \tilde{N}^*(\Omega_h) \tilde{N}(\Omega_k) \rangle = \frac{2\pi\nu}{nT} \delta_{h,k}. \quad (56)$$

A faithful detection of the phase modulation at angular frequency Ω_k requires that the signal in Eq. (54) is much larger than the noise,

$$\langle |\tilde{N}(\Omega_k)|^2 \rangle \ll |\Omega_k|^2 |\tilde{\varphi}(\Omega_k)|^2. \quad (57)$$

By using Eq. (56) for $h = k$ into Eq. (57), solving for ν and defining $T_{\text{win}} = nT$ as the amplitude of the time window of the Fourier transform and $f_k = \Omega_k/(2\pi)$ as the frequency in hertz, Eq. (57) yields

$$\nu \ll 2\pi |f_k|^2 |\tilde{\varphi}(2\pi f_k)|^2 T_{\text{win}}. \quad (58)$$

This equation gains clarity when we define $T_k = 1/f_k$ as the period of the spectral component with frequency f_k , becoming

$$\nu \ll 2\pi |f_k| |\tilde{\varphi}(2\pi f_k)|^2 \frac{T_{\text{win}}}{T_k}. \quad (59)$$

The conditions stated by Eqs. (58) and (59) are independent of the sampling time T and the number of samples n (provided that $n \gg 1$). Specifically, Eq. (59) illustrates that the maximum tolerable linewidth is directly proportional to the modulation frequency, the amplitude square of the phase modulation and the ratio T_{win}/T_k , which is the number of temporal periods contained within the time window of the Fourier transform $T_{\text{win}} = nT$. Therefore, widening the time window of the short-time Fourier transform T_{win} can alleviate the requirements on the laser linewidth compared to the detection of transient phase deviations discussed earlier in this section. However, this can only be achieved by sacrificing temporal resolution, which is determined by the amplitude of the time window T_{win} . Consequently, the necessity of using ultra-stable lasers for detecting low intensity sub-hertz signals persists even with approaches based on the short-time Fourier transform.

The independence of Eqs. (58) and (59) on the sampling time T and the number of samples n suggests that these equations are also valid in the continuous limit where n tends to infinity and T to zero, with their product $T_{\text{win}} = nT$ finite. The derivation of Eqs. (58) and (59) in the continuous case is presented in appendix A.

V. POLARIZATION-BASED SENSING

Now, let us explore the potential of the use of polarization for sensing. The prominent advantage of polarization compared to phase is that polarization is unaffected by laser phase noise. This characteristic makes polarization the preferred choice for detecting environmental processes with very low

frequencies. Let us now analyze how polarization can be used for sensing with the help of the theory established in the previous sections.

The solution of (27) is the concatenation of infinitesimal rotations around the axes $\vec{\beta}(z)dz$. For sensing, we are interested into the change of the state of polarization induced by small time-dependent changes $\Delta\vec{\beta}(z, t)$ of $\vec{\beta}$

$$\frac{d\mathbf{U}(z, t)}{dz} = \frac{i}{2} [\vec{\beta}(z) + \Delta\vec{\beta}(z, t)] \cdot \vec{\sigma} \mathbf{U}(z, t). \quad (60)$$

Let us now use an approach is similar to the interaction picture in quantum mechanics, separating the “free” static evolution from the “interaction” time-dependent part.¹⁰ To this purpose, let us represent $\mathbf{U}(z, t)$ as the concatenation of two unitary matrices

$$\mathbf{U}(z, t) = \mathbf{U}_0(z) \mathbf{U}_1(z, t). \quad (61)$$

The matrix $\mathbf{U}(z, t)$ is solution of Eq. (60) if $\mathbf{U}_0(z, t)$ and $\mathbf{U}_1(z, t)$ satisfy the equations

$$\frac{d\mathbf{U}_0(z)}{dz} = \frac{i}{2} \vec{\beta}(z) \cdot \vec{\sigma} \mathbf{U}_0(z), \quad (62)$$

$$\frac{d\mathbf{U}_1(z, t)}{dz} = \frac{i}{2} \left\{ \mathbf{U}_0^{-1}(z) [\Delta\vec{\beta}(z, t) \cdot \vec{\sigma}] \mathbf{U}_0(z) \right\} \mathbf{U}_1(z, t). \quad (63)$$

Equation (63) is equivalent to

$$\frac{d\mathbf{U}_1(z, t)}{dz} = \frac{i}{2} \left\{ \left[\mathbf{R}_0^{-1}(z) \Delta\vec{\beta}(z, t) \right] \cdot \vec{\sigma} \right\} \mathbf{U}_1(z, t), \quad (64)$$

where $\mathbf{R}_0(z)$ is the rotation operator in Stokes space corresponding to the unitary operator $\mathbf{U}_0(z)$ in Jones space by the relation $\mathbf{R}_0(z) \vec{\sigma} = \mathbf{U}_0^{-1}(z) \vec{\sigma} \mathbf{U}_0(z)$. By doing so, we employ a frame that rotates with the static birefringence $\vec{\beta}(z)$, effectively eliminating the static, z -dependent rotations induced by $\vec{\beta}(z)$.¹² In this reference frame, the state of polarization becomes in terms of the original one $\vec{s}' = \mathbf{R}_0^{-1}(z) \vec{s}$, and the evolution of the polarization vector \vec{s}' is described by the equation

$$\frac{d\vec{s}'}{dz} = \Delta\vec{\beta}'(z, t) \times \vec{s}', \quad (65)$$

where

$$\Delta\vec{\beta}'(z, t) = \mathbf{R}_0^{-1}(z) \Delta\vec{\beta}(z, t). \quad (66)$$

This equation shows that when perturbations are absent and therefore $\Delta\vec{\beta}'(z, t) \equiv 0$, we have $d\vec{s}'/dz \equiv 0$ and hence $\vec{s}' \equiv \vec{s}_0$, where \vec{s}_0 is the input Stokes vector (which is identical in the rotating frame and in the original frame). If the fluctuations of the birefringence are sufficiently small such that their impact on \vec{s}' is linear – a prerequisite for ensuring linearity of the sensing mechanism – a perturbative approach can be applied around the unperturbed solution $\vec{s}' = \vec{s}_0$. This involves setting $\vec{s}(z, t) = \vec{s}_0 + \Delta\vec{s}(z, t)$ with $\Delta\vec{s}(z, t)$ of the same order of $\Delta\vec{\beta}'(z, t)$, leading to

$$\frac{d\Delta\vec{s}'}{dz} = \Delta\vec{\beta}'(z, t) \times \vec{s}_0. \quad (67)$$

Integration of the above gives

$$\Delta \vec{s}'(z, t) = \int_0^z \Delta \vec{\beta}'(z', t) dz' \times \vec{s}_0, \quad (68)$$

where $\Delta \vec{s}'(z, t) = \vec{s}'(z, t) - \vec{s}_0$ is the deviation of the rotated state of polarization from the static position.

Let us now use the general relations that we have just derived first considering the case in which the perturbation is caused by strain. In this case we have

$$\Delta \vec{s}'(z, t) = \xi \int_0^z \varepsilon(z', t) \vec{\beta}'_{\perp}(z') dz', \quad (69)$$

where we have defined $\Delta \vec{\beta}'_{\perp}(z) = \Delta \vec{\beta}'(z, t) \times \vec{s}_0$, the component of $\Delta \vec{\beta}'(z, t)$ perpendicular to \vec{s}_0 and rotated around \vec{s}_0 by 90° . Similarly to phase deviations, the deviation of the state of polarization from its steady-state value is proportional to $\varepsilon(z', t)$, ensuring the linearity of the sensing probe. However, the behavior differs when it comes to signal accumulation. Unlike the deterministic nature of the polarization averaged birefringence vector, which is uniform in space in the absence of perturbations, in standard single mode fibers, the pre-existing birefringence varies randomly over a scale of tens of meters. Fortunately, however, a simplification arises from the fact that external perturbations generally occur on orders of magnitude larger scales, making it appropriate to perform statistical averaging over the short-scale variation of the birefringence. As we will demonstrate below, this results in the accumulation of the deviation of the state of polarization along the fiber being incoherent, contrasting with the coherent accumulation of phase deviations.

A realistic birefringence correlation function is

$$\langle \vec{\beta}(z) \cdot \vec{\beta}(z') \rangle = \langle \beta^2 \rangle \exp(-|z - z'|/L_f), \quad (70)$$

where L_f , the birefringence correlation length, is of the order of meters.¹³ Assuming that the scale of variation of the external perturbation is much longer, it is appropriate to replace right hand side of the above with a Dirac delta function of equal area

$$\langle \vec{\beta}(z) \cdot \vec{\beta}(z') \rangle = 2L_f \langle \beta^2 \rangle \delta(z - z'). \quad (71)$$

The fiber birefringence $\vec{\beta}(z)$ represents linear birefringence and therefore belongs to the equatorial plane of the Stokes space. Conversely, in the rotated reference frame the rotated birefringence $\vec{\beta}'(z) = \mathbf{R}_0^{-1}(z) \vec{\beta}(z)$ is instead isotropically distributed because $\mathbf{R}_0^{-1}(z)$ it is the concatenation of rotations with axes $\vec{\beta}(z)$ that vary over a length scale of few meters, so that its components are uncorrelated to each other and each one has a variance one third of the total. Consequently we have

$$\langle \vec{\beta}'_{\perp}(z) \cdot \vec{\beta}'_{\perp}(z') \rangle = \frac{2}{3} \langle \vec{\beta}(z) \cdot \vec{\beta}(z') \rangle. \quad (72)$$

Using now Eq. (69) we obtain

$$\langle \Delta \vec{s}'(z, t) \cdot \Delta \vec{s}'(z', t') \rangle = \frac{4}{3} \langle \beta^2 \rangle L_f \xi^2 \int_0^z \varepsilon(z, t) \varepsilon(z', t') dz'. \quad (73)$$

The contribution of a fiber section to the fluctuations of the polarization are proportional to the strength of the local static birefringence, which is a quantity well characterized in optical fibers because the fiber's polarization mode dispersion depends on it. The fiber polarization mode dispersion is related to $\langle \beta^2 \rangle L_f$ by

$$\langle \tau^2 \rangle = \frac{1}{\omega_0^2} 2L_f \langle \beta^2 \rangle z, \quad (74)$$

with $\langle \tau \rangle^2 = 8 \langle \tau^2 \rangle / (3\pi)$ the mean polarization mode dispersion square.¹³ If we define as $\kappa^2 = \langle \tau \rangle^2 / z$ the averaged square polarization mode dispersion of the fiber in ps/ $\sqrt{\text{km}}$, we may eliminate $2L_f \langle \beta^2 \rangle$ in the correlation functions by using

$$2L_f \langle \beta^2 \rangle = \frac{3\pi \omega_0^2 \kappa^2}{8}. \quad (75)$$

After using $\omega_0 = 2\pi c / \lambda$, we obtain

$$\langle \Delta \vec{s}'(z, t) \cdot \Delta \vec{s}'(z', t') \rangle = \frac{\pi}{4} \left(\frac{2\pi c}{\lambda} \right)^2 \kappa^2 \xi^2 \int_0^z \varepsilon(z, t) \varepsilon(z', t') dz', \quad (76)$$

Let us now analyze twist. Combining Eqs. (37), (66) and (68), yields

$$\Delta \vec{s}'(z, t) = \int_0^z 2\alpha(z', t) \mathbf{R}_0^{-1}(z') [\hat{e}_3 \times \vec{\beta}(z')] dz' \times \vec{s}_0. \quad (77)$$

The outcome of $\hat{e}_3 \times \vec{\beta}(z)$ yields a vector with the same magnitude as $\vec{\beta}(z)$ but rotated by 90° in the equatorial plane. Considering that $\vec{\beta}(z)$ lies within the equatorial plane and is distributed isotropically, the result of this rotation is statistically equivalent to $\vec{\beta}(z)$. Consequently, we can substitute $\mathbf{R}_0^{-1}(z') [\hat{e}_3 \times \vec{\beta}(z')]$ with $\vec{\beta}'(z)$ and proceed along the same route of the analysis for strain. The final result is

$$\langle \Delta \vec{s}'(z, t) \cdot \Delta \vec{s}'(z', t') \rangle = \frac{4}{3} \langle \beta^2 \rangle L_f \int_0^z 4\alpha(z', t) \alpha(z', t') dz', \quad (78)$$

and, using Eq. (75)

$$\langle \Delta \vec{s}'(z, t) \cdot \Delta \vec{s}'(z', t') \rangle = \frac{\pi}{4} \left(\frac{2\pi c}{\lambda} \right)^2 \kappa^2 \int_0^z 4\alpha(z', t) \alpha(z', t') dz'. \quad (79)$$

As discussed in ref. 4, strain is most likely the predominant source of perturbation in submarine systems employing jelly-filled cables, while twist has a dominant role in aerial cables exposed to wind.¹⁴

It is important to note that, in both cases of strain and twist, the temporal correlation functions of the deviations of the state of polarization are proportional to the temporal correlation functions of the perturbations, integrated over the entire link length. This property insures that the spectrum of the fluctuations of the state of polarization faithfully reproduces the spectrum of the integrated strain and twist. Additionally, in both cases, the sensitivity is proportional to the polarization mode dispersion coefficient of the fiber.

With polarization, the spectra are obtained in terms of ensemble averages. It is well established¹⁵ that polarization fluctuations exhibit ergodic behavior in frequency, meaning that ensemble averages can be effectively replaced by averages over frequency, if taken over a bandwidth containing a sufficient number of principal state of polarization bandwidths. In this particular scenario, however, measurement data over a sufficiently large frequency span are not easily accessible, but fortunately, they are also unnecessary. This is because the length scale of the environmental perturbations, of the order of tens of kilometers, is much greater than the length scale of the spatial variations of the birefringence, of the order of tens of meters. Consequently, significant self averaging of the birefringence fluctuations occurs over the length scale of the environmental perturbations. This issue will be further discussed and the effectiveness of self averaging validated against experimental data in Sec. IX, where we analyze a few cases of earthquakes and sea swell detection.

VI. COMPARISON BETWEEN PHASE AND POLARIZATION ACCUMULATION

Let us now compare the signal accumulation between polarization and phase deviations, limiting ourselves to the case in which the perturbation is due to strain because twist is uncoupled to phase. If we compare Eq. (76) and that obtained from Eq. (39)

$$\Delta\varphi(z,t)\Delta\varphi(z,t') = \left(\frac{2\pi}{\lambda}\right)^2 n_0^2 \xi^2 \int_0^z \int_0^z \varepsilon(z',t)\varepsilon(z'',t')dz'dz'', \quad (80)$$

we notice that, although both $\langle \Delta\vec{s}(z,t) \cdot \Delta\vec{s}(z,t') \rangle$ and $\Delta\varphi(z,t)\Delta\varphi(z,t')$ are proportional to the *temporal* correlation function of the strain, the accumulation of the strain contributions along the fiber is different in the two cases. For polarization, sections with positive and negative strain give the same contribution to signal strength, because $\langle |\Delta\vec{s}(z,t)|^2 \rangle$ depends only on $\varepsilon(z,t)^2$. On the contrary, Eq. (39) reveals that sections subjected to positive strain yield a positive contribution to the phase deviations, while sections experiencing negative strain contribute negatively, thus partially offsetting each other's effects.

To get an order of magnitude estimate of the effect that averaging produces on phase measurements, let us assume a seismic wave of wavelength Λ whose amplitude is modulated by the envelope $\varepsilon_0(z,t)$, namely $\varepsilon(z,t) = \sin(2\pi z/\Lambda)\varepsilon_0(z,t)$. With this assumption, Eq. (39) becomes

$$\Delta\varphi(z,t) = \frac{2\pi}{\lambda} n_0 \int_0^z \xi \cos(2\pi z'/\Lambda) \varepsilon_0(z',t) dz', \quad (81)$$

that is

$$\Delta\varphi(z,t) = \frac{2\pi}{\lambda} n_0 \xi \tilde{\varepsilon}_0(2\pi/\Lambda, t), \quad (82)$$

where

$$\tilde{\varepsilon}_0(K,t) = \frac{1}{2} \text{Re} \left[\int_{-\infty}^{\infty} \exp(-iKz) \varepsilon_0(z',t) dz' \right], \quad (83)$$

is the spatial Fourier transform of the strain perturbation (which we assume zero outside the fiber length) calculated at the spatial wavevector $K = 2\pi z/\Lambda$. Assuming for the envelope of the perturbation $\varepsilon_0(z',t)$ a Gaussian distribution of root mean square L_0 entirely contained into the fiber length

$$\varepsilon_0(z,t) = \varepsilon_0 \exp\left(-\frac{z^2}{2L_0^2}\right), \quad (84)$$

we obtain

$$\tilde{\varepsilon}_0(K,t) = \frac{\sqrt{2\pi}}{2} L_0 \varepsilon_0 \exp\left(-\frac{2\pi^2 L_0^2}{\Lambda^2}\right). \quad (85)$$

The wavelength of seismic waves Λ_0 is of the order of 100 km, but if we assume a plane seismic wave incident on the local direction of the cable with an angle ϑ , the spatial periodicity is $\Lambda = \Lambda_0/\cos\vartheta$, so it is in general larger than Λ_0 and equal only if the wavevector of the seismic wave is parallel to the direction of the cable. With this simplified assumption we obtain

$$\Delta\varphi(z,t) = \frac{2\pi}{\lambda} n_0 \xi \frac{\sqrt{2\pi}}{2} L_0 \varepsilon_0 \exp\left(-\cos^2\vartheta \frac{2\pi^2 L_0^2}{\Lambda_0^2}\right). \quad (86)$$

Notice the dependence on $\cos^2\vartheta$ at the exponent, suggesting a larger sensitivity for seismic wave approximately orthogonal to the cable, consistent with experimental observations detailed in ref. 16. For comparison, with polarization

$$\langle |\Delta\vec{s}(z,t)|^2 \rangle^{1/2} = \frac{\sqrt{\pi}}{2} \frac{2\pi c}{\lambda} \kappa \xi \left[\int_0^z \varepsilon(z,t)^2 dz' \right]^{1/2}, \quad (87)$$

that is, with the Gaussian assumption and assuming $\Lambda \ll L_0$ so that we may replace the cosine square with its average one half,

$$\langle |\Delta\vec{s}(z,t)|^2 \rangle^{1/2} = \frac{\sqrt{\pi}}{2} \frac{2\pi c}{\lambda} \kappa \xi \varepsilon_0 \left(\frac{\sqrt{2\pi} L_0}{4} \right)^{1/2}. \quad (88)$$

Comparing the two signals, we have

$$\Delta\varphi(z,t) = \left(\frac{32}{\pi}\right)^{1/4} \frac{n_0 \sqrt{L_0}}{\kappa c} \exp\left(-\cos^2\vartheta \frac{2\pi^2 L_0^2}{\Lambda_0^2}\right) \langle |\Delta\vec{s}(z,t)|^2 \rangle^{1/2}. \quad (89)$$

Introducing the full-width at half maximum of a Gaussian $L_f = 2\sqrt{2\ln(2)}L_0$

$$\Delta\varphi(z,t) = 4 \left(\frac{\ln 2}{\pi}\right)^{1/4} \frac{n_0 \sqrt{L_f}}{\kappa c} \exp\left(-\cos^2\vartheta \frac{\pi^2 L_f^2}{4\Lambda_0^2 \ln 2}\right) \langle |\Delta\vec{s}(z,t)|^2 \rangle^{1/2}. \quad (90)$$

Assuming $\kappa = 0.03 \text{ ps}/\sqrt{\text{km}}$ and $n_0 = 1.5$, we obtain for $L_f = 2\Lambda_0/\cos\vartheta$ and $L_f = 400 \text{ km}$, $\Delta\phi(z, t) \simeq 6000 \langle |\Delta\vec{s}(z, t)|^2 \rangle^{1/2}$ rad. When the ratio $L_f/(\Lambda/\cos\vartheta)$ becomes larger, the efficiency of the phase modulation drops very rapidly as a consequence of the Gaussian profile and the fact that we assumed Λ as a constant, so that the expression may become meaningless in this limit.

The root mean square deviations of the signal polarization being much smaller than the amplitude of the phase deviations ensures that the polarization deviations fall within the linear range even for very large external perturbations, like those applied by earthquakes of high magnitudes, as we will show in section IX.

VII. THE JONES MATRIX IN THE ROTATING FRAME

In the rotating frame in which the static birefringence is removed, the Jones matrix can be represented, similarly to Eq. (22), as

$$\mathbf{U}_1(t) = \exp \left[\frac{i}{2} \Delta\vec{\phi}'(t) \cdot \vec{\sigma} \right]. \quad (91)$$

In the same frame, the output Stokes vector is

$$\vec{s}'(t) = \langle \vec{s}_0 | \mathbf{U}_1^\dagger(t) \vec{\sigma} \mathbf{U}_1(t) | \vec{s}_0 \rangle = \exp [\Delta\vec{\phi}'(t) \times] \vec{s}_0. \quad (92)$$

Being in the cases of interest for sensing $|\Delta\vec{\phi}'(t)| \ll \pi$, because otherwise the probe does not depend linearly on the perturbations, we may expand the exponential in the last member of Eq. (92) to first order obtaining for $\Delta\vec{s}(t) = \vec{s}'(t) - \vec{s}_0$

$$\Delta\vec{s}'(t) = \Delta\vec{\phi}(t) \times \vec{s}_0. \quad (93)$$

If we use the expression of $\Delta\vec{s}'(t)$ given by Eq. (68) we get¹⁷

$$\Delta\vec{\phi}(t) = \int_0^z \Delta\vec{\beta}'(z', t) dz'. \quad (94)$$

Comparison of Eqs. (91) with Eq. (93) reveals that the detection of the fluctuations of the output polarization from the average value, $\Delta\vec{s}'(t)$, with a fixed input enables the characterization of the fluctuations of two out of the three parameters that identify the Jones matrix of the link, the two components of $\Delta\vec{\phi}(t)$ orthogonal to \vec{s}_0 .¹⁷

The three components of $\Delta\vec{\phi}(t)$ and hence a complete characterization of the fluctuations of the rotation vector can be obtained from $\mathbf{U}_1(t)$ with the following procedure. A coherent receiver reconstructs the Jones matrix in the original frame, $\mathbf{U}(t)$. Using Eq. (61), we find that $\mathbf{U}_1(t)$ is related to $\mathbf{U}(t)$ by the following equation

$$\mathbf{U}_1(t) = \mathbf{U}_0^{-1} \mathbf{U}(t). \quad (95)$$

In practical terms, the Jones matrix in the rotating frame can be extracted by left-multiplying the Jones matrix directly obtained from the receiver, $\mathbf{U}(t)$, by the inverse of the “static” Jones matrix, \mathbf{U}_0 .¹⁷ The latter is obtained by averaging the Jones matrix $\mathbf{U}(t)$ over a sufficiently long time window. The

duration of the averaging time window sets the lower limit on the bandwidth of $\Delta\vec{\phi}(t)$. Once $\mathbf{U}_1(t)$ is extracted, we obtain

$$\Delta\vec{\phi}(t) = \text{trace} \{ -i \log [\mathbf{U}_1(t)] \vec{\sigma} \}. \quad (96)$$

Whether the polarization state corresponding to a fixed input is measured, or the Jones matrix is reconstructed from the receiver, to achieve a linear dependency of the measured quantity on the applied strain both approaches require employing of a frame that rotates with the static birefringence, and both approaches yield identical results. When utilizing a fixed polarization at the input, as done in refs. 3 and 4, one extracts the two components of $\int_0^z dz' \Delta\vec{\beta}'(z', t)$ orthogonal to the input polarization \vec{s}_0 .¹⁷ Conversely, knowledge of the full Jones matrix provides access to all three components of $\int_0^z dz' \Delta\vec{\beta}'(z', t)$.

VIII. LOCALIZATION WITH POLARIZATION

The integral in $\Delta\vec{\phi}(t)$ can be readily obtained in transmission experiments^{4,17}. However, in such experiments, only the perturbation accumulated over the entire link can be extracted. Below, we outline a procedure demonstrating that in experiments utilizing time-resolved backscattering, such as in distributed acoustic sensing, or in experiments employing high-loss loopbacks as in ref. 18–21, it is possible to extract one of the three components of $\Delta\vec{\phi}(t)$ specific to a section located at any position along the link.

Assume that \mathbf{U}_f is the Jones matrix that describes the evolution of the polarization of a single mode fiber up to a given distance z and $\Delta\mathbf{U}$ the unitary matrix describing the evolution in a section that goes from z to $z + \Delta z$ along the same fiber, which we will refer to as the section of interest in the following. Then, the backscattered field is either rerouted through a different fiber with Jones matrix \mathbf{U}_b or transmitted back through the same fiber, in which case $\mathbf{U}_b = \mathbf{U}_f$. The Jones matrix $\mathbf{U}_{rt}(1)$ describing the round-trip propagation from 0 to z and back, and the Jones matrix $\mathbf{U}_{rt}(2)$ describing the round-trip propagation from 0 to $z + \Delta z$ and back, are²²

$$\mathbf{U}_{rt}(1) = \mathbf{U}_b^T \mathbf{U}_f, \quad (97)$$

$$\mathbf{U}_{rt}(2) = \mathbf{U}_b^T (\Delta\mathbf{U}^T \Delta\mathbf{U}) \mathbf{U}_f, \quad (98)$$

where the superscript T stands for transpose. Our aim is to characterize the unitary matrix

$$\Delta\mathbf{U}_{rt} = \Delta\mathbf{U}^T \Delta\mathbf{U}, \quad (99)$$

from a measurement of $\mathbf{U}_{rt}(1)$ and $\mathbf{U}_{rt}(2)$. Left multiplying by $\mathbf{U}_{rt}^{-1}(1)$ both sides of the above, we obtain

$$\mathbf{U}_{\text{meas}} = \mathbf{U}_f^{-1} \Delta\mathbf{U}_{rt} \mathbf{U}_f, \quad (100)$$

where we have defined the unitary matrix

$$\mathbf{U}_{\text{meas}} = \mathbf{U}_{rt}(1)^{-1} \mathbf{U}_{rt}(2). \quad (101)$$

From now on, we will assume that \mathbf{U}_{meas} has been characterized experimentally and is known. Let us now define

$$\mathbf{U}_{\text{meas}} = \exp(i\vec{\phi}_{\text{meas}}/2 \cdot \vec{\sigma}), \quad (102)$$

$$\mathbf{U}_f = \exp(i\vec{\phi}_f/2 \cdot \vec{\sigma}), \quad (103)$$

and

$$\Delta\mathbf{U}_{\text{rt}} = \exp[(\Delta\vec{\phi}_0 + \Delta\vec{\phi}_1)/2 \cdot \vec{\sigma}], \quad (104)$$

where $\Delta\vec{\phi}_0$ is the contribution of the static birefringence in the section of interest and $\Delta\vec{\phi}_1$ of the perturbation. Entering the above definitions into Eq. (100) we obtain

$$\vec{\phi}_{\text{meas}} = \exp(-\vec{\phi}_f \times)(\Delta\vec{\phi}_0 + \Delta\vec{\phi}_1). \quad (105)$$

The vector $\vec{\phi}_{\text{meas}}$ can be extracted from the measurement data using

$$\vec{\phi}_{\text{meas}} = \text{trace}[-i \log(\mathbf{U}_{\text{meas}}) \vec{\sigma}]. \quad (106)$$

Taking the modulus square of both terms of (105) yields

$$|\vec{\phi}_{\text{meas}}|^2 = |\Delta\vec{\phi}_0 + \Delta\vec{\phi}_1|^2 = |\Delta\vec{\phi}_0|^2 + |\Delta\vec{\phi}_1|^2 + 2\Delta\vec{\phi}_0 \cdot \Delta\vec{\phi}_1. \quad (107)$$

In this equation $\Delta\vec{\phi}_0$ is time independent whereas $\Delta\vec{\phi}_1$ is time-dependent. The technique used in ref. 20 and 21 was based on the analysis of the temporal modulation of $|\vec{\phi}_{\text{meas}}|^2$ or its square root. In both cases, this approach fails to return the spectrum of the perturbation because the term $|\Delta\vec{\phi}_1|^2$ is non-linear in the perturbation and is generally not negligible compared to the linear term $\Delta\vec{\phi}_0 \cdot \Delta\vec{\phi}_1$. This is because, although the birefringence is much larger than its fluctuations, being $\Delta\phi_0 \leq \pi$ for the periodicity of rotations, the vectors $\Delta\vec{\phi}_0$ and $\Delta\vec{\phi}_1$ have comparable magnitudes. Consequently, the temporal variations of the length of the rotation vector are generally not proportional to any of the components of $\Delta\vec{\phi}_1$, which are the quantities of interest because related to the fiber strain in the section of interest. However, we will show in the remainder of this section that further manipulations of the above equations enable the establishment of a procedure for extracting one of the three components of $\Delta\vec{\phi}_1$.

If we insert into Eq. (100) the decomposition $\mathbf{U}_f = \mathbf{U}_{0,f} \mathbf{U}_{1,f}$, where $\mathbf{U}_{0,f}$ is the static contribution and $\mathbf{U}_{1,f}$ the contribution of the perturbations of the forward propagation, Eq. (100) becomes

$$\mathbf{U}_{\text{meas}} = \mathbf{U}_{1,f}^{-1} \Delta\mathbf{U}'_{\text{rt}} \mathbf{U}_{1,f}, \quad (108)$$

where

$$\Delta\mathbf{U}'_{\text{rt}} = \mathbf{U}_{0,f}^{-1} \Delta\mathbf{U}_{\text{rt}} \mathbf{U}_{0,f} \quad (109)$$

is the Jones matrix of the roundtrip propagation through the section under test rotated by the *static* birefringence of the forward propagation. Let us define, using the prime for the quantities rotated by the static birefringence,

$$\Delta\mathbf{U}'_{\text{rt}} = \exp[i(\Delta\vec{\phi}'_0 + \Delta\vec{\phi}'_1)/2 \cdot \vec{\sigma}], \quad (110)$$

where $\Delta\vec{\phi}'_0$ is the contribution of the static birefringence in the section under test and $\Delta\vec{\phi}'_1$ of the perturbations, rotated by the static birefringence of the forward propagation, and represent $\mathbf{U}_{1,f}$ as

$$\mathbf{U}_{1,f} = \exp(i\vec{\phi}'_{1,f}/2 \cdot \vec{\sigma}). \quad (111)$$

If we now use Eq. (108), we may express the matrix \mathbf{U}_{meas} as⁹

$$\mathbf{U}_{\text{meas}} = \exp[i\mathbf{R}_{1,f}(\Delta\vec{\phi}'_0 + \Delta\vec{\phi}'_1)/2 \cdot \vec{\sigma}], \quad (112)$$

where

$$\mathbf{R}_{1,f} = \exp(-\vec{\phi}_{1,f} \times) \simeq \mathbb{1} - \vec{\phi}_{1,f} \times \quad (113)$$

where we used that $\vec{\phi}_{1,f} \ll \pi$ because it is produced by the small perturbations in the forward propagation. Comparing Eq. (102) with Eq. (112) we obtain

$$\vec{\phi}_{\text{meas}} = \Delta\vec{\phi}'_0 + \Delta\vec{\phi}'_1 - \vec{\phi}_{1,f} \times \Delta\vec{\phi}'_0 - \vec{\phi}_{1,f} \times \Delta\vec{\phi}'_1. \quad (114)$$

The terms $\Delta\vec{\phi}'_1$ and $\vec{\phi}_{1,f}$ are small time-dependent perturbations in the section of interest and in the forward propagation. If we average them over a sufficiently long time interval these terms vanish, so that we have

$$\mathbb{E}(\vec{\phi}_{\text{meas}}) = \Delta\vec{\phi}'_0. \quad (115)$$

If we now define

$$\Delta\vec{\phi}_{\text{meas}} = \vec{\phi}_{\text{meas}} - \mathbb{E}(\vec{\phi}_{\text{meas}}), \quad (116)$$

we have

$$\Delta\vec{\phi}_{\text{meas}} = \Delta\vec{\phi}'_1 - \vec{\phi}_{1,f} \times \Delta\vec{\phi}'_0 - \vec{\phi}_{1,f} \times \Delta\vec{\phi}'_1. \quad (117)$$

Being the term $\vec{\phi}_{1,f} \times \Delta\vec{\phi}'_1$ the product of perturbation terms which we may assume much smaller than one, it can be neglected with respect to linear terms, so that the equation above, solved for $\Delta\vec{\phi}'_1$, gives

$$\Delta\vec{\phi}'_1 \simeq \Delta\vec{\phi}_{\text{meas}} - \vec{\phi}'_{1,f} \times \Delta\vec{\phi}'_0. \quad (118)$$

In Eq. (118), $\Delta\vec{\phi}'_0$ is the known, time independent, rotation vector given by Eq. (115), accounting for the effect of the static birefringence in the round-trip through the section under test, $\vec{\phi}'_{1,f}$ is the (unknown) time-dependent result of the birefringence perturbations in the forward propagation up to z , and

$$\Delta\vec{\phi}'_1 = \int_z^{z+\Delta z} \Delta\vec{\beta}'_f(z', t) dz' + \int_{z+\Delta z}^z \Delta\vec{\beta}'_b(z', t) dz' \quad (119)$$

is the time-dependent birefringence accumulated over the roundtrip from z to $z + \Delta z$ rotated by the static birefringence of the forward propagation up to z .

Equation (118) states that the three components of $\Delta\vec{\phi}'_1$ are equal to the known vector $\Delta\vec{\phi}_{\text{meas}}$ corrupted by an extra term involving the unknown time-dependent vector $\vec{\phi}'_{1,f}$. One of the three components of $\Delta\vec{\phi}'_1$ is however unaffected by the extra term. Specifically, if we project $\Delta\vec{\phi}_{\text{meas}}$ over the direction parallel to $\hat{e}_0 = \Delta\vec{\phi}'_0/\Delta\phi'_0$, we obtain

$$\Delta\vec{\phi}'_1 \cdot \hat{e}_0 = \Delta\vec{\phi}_{\text{meas}} \cdot \hat{e}_0. \quad (120)$$

Projection over the direction of $\Delta\vec{\phi}'_0$ allows the separation of the time-dependent fluctuations of the polarization caused by the birefringence perturbations in the section of interest from those originating from the light propagation before the section of interest. Although only a single component of the integrated birefringence fluctuations can be extracted by this procedure, this is sufficient to derive the strain perturbation spectrum due to the isotropic nature of $\Delta\vec{\phi}'_1$. The isotropy of the polarization fluctuations will be corroborated through the analysis of experimental data in the following section.

As a final comment, we notice that the procedure that we have just described is equivalent to subtract the steady state value of the rotation matrix by a procedure similar to that described and experimentally validated in ref. 17. That approach, in turn, was equivalent to the rotation used in ref. 4 to align the average of the output polarization with the north pole of the Poincaré sphere. This alignment was crucial for establishing a correspondence between the spectrum of polarization fluctuations and the spectra of earthquakes and microseisms in ref. 3.

IX. ENVIRONMENTAL SENSING USING THE STATE OF POLARIZATION

In this section, we explore the potential of utilizing the state of polarization as a sensing probe for detecting earthquakes and sea swells in proximity to an optical cable. We will make extensive use of the database of Ref. 1, demonstrating how the analysis of the correlation between measurements obtained from two wavelength division multiplexing channels offers valuable insights, potentially enabling a coarse localization of earthquake events.

Fibers embedded in loose tube gel-filled cables laid on the seafloor experience a static pressure of about 10^5 Pa every 10 meters of depth. For a 4-kilometer depth (the average depth of the Curie cable³), the pressure is approximately 400×10^5 Pa, roughly 400 times atmospheric pressure. This static pressure induces strain due to the Poisson effect. During an oceanic earthquake, the movement of the seafloor causes the water column above the cable to oscillate. The inertia of this water column leads to fluctuations in the pressure acting on the cable around its static value. Consequently, these pressure fluctuations induce oscillations in strain, affecting both the polarization-averaged propagation constant and the birefringence of the fiber.

We will analyze data from two channels, denominated channel 1 and channel 2 in Ref. 1, belonging to the Curie submarine cable system, connecting Los Angeles, California, to Valparaiso, Chile, for a total of 10,500 km of length. In the measurement campaign, both channels were looped back in Valparaiso, so that the signals were transmitted and received in Los Angeles, covering a total round-trip distance of 21,000 km. Channel 1 operated at a frequency centered at 193.5805 THz, while channel 2 operated at 193.6570 THz, resulting in a frequency separation of $\Delta f = 76.5$ GHz (see the supplementary material of ref. 3 for details).

The database of ref. 1 provides the three components of the

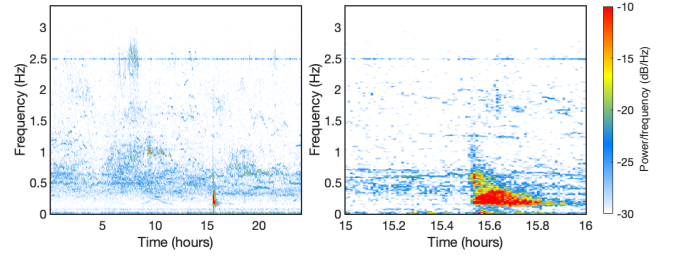


FIG. 1. Sum of the spectrograms of the two components of $\Delta\vec{s}$ orthogonal to \vec{s}_0 of channel 1, referring to an M7.3 earthquake that occurred in Oaxaca on June 23, 2020, at UTC time 15:29:05. The horizontal axis represents UTC time. The left panel depicts the entire day of the earthquake, while the right panel zooms in on a one-hour time window around the earthquake event.

Stokes vector rotated such that the Stokes vectors averaged over a 200 s time window coincide with the north pole of the Poincaré sphere. From now on, we will refer to these components as if they were those in the frame rotating with the static fiber birefringence. Although in the field experiment the input to the fiber was a fixed linear polarization,¹⁷ hence a point on the equator of the sphere, this equivalence is justified by the fact that the constant rotation from the fixed point on the equator to the north pole does not impact the time-dependent deviations from the average polarization. It should be noted, however, that the rotation of the sphere that aligns the average polarization to a fixed point of the sphere does not specify the orientation of the sphere around the average point. The rotating frame is therefore undetermined for a rotation of the cloud of polarization points around the average. This indetermination does not affect accuracy when polarization dependent loss is negligible as assumed in our analysis, because in this case the fluctuations of the deviations of the Stokes vector from the average Stokes vector are isotropic.

Figure 1 displays the sum of the spectrograms of the two components of $\Delta\vec{s}$ orthogonal to \vec{s}_0 of channel 1, concerning an M7.3 earthquake that took place in Oaxaca on June 23, 2020, at UTC time 15:29:05. The horizontal axis represents UTC time. The left panel illustrates the entire day of the earthquake, while the right panel zooms in on a one-hour time window around the earthquake occurrence.

Figure 2 illustrates the spectrograms of the two components of the deviations of the Stokes vector separately. It is noteworthy that both spectrograms display similar spectral features, despite the random nature of the birefringence acting independently on each component. This independence is confirmed by the observation that the magnitude of the cross-correlation between the two components does not exceed 5%. This similarity strongly suggests that, as we anticipated at the end of section V, significant spatial self averaging occurs, and therefore the random nature of the static birefringence does not impose a significant limitation on the accuracy of sensing approaches based on the analysis of the modulation of the state of polarization at the output of a long fiber with random birefringence.

Figure 3 depicts the temporal traces of the two components

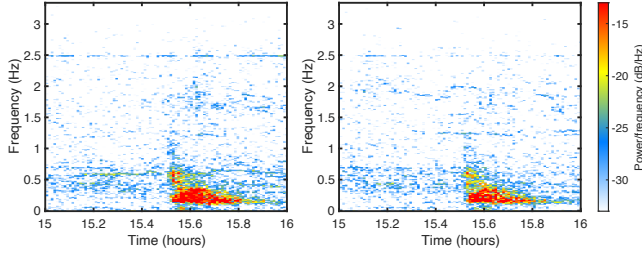


FIG. 2. Spectrograms of the two components of $\Delta\vec{s}$ orthogonal to \vec{s}_0 relative to a M7.3 earthquake occurred in Oaxaca on 23 June 2020, UTC time 15:29:05.

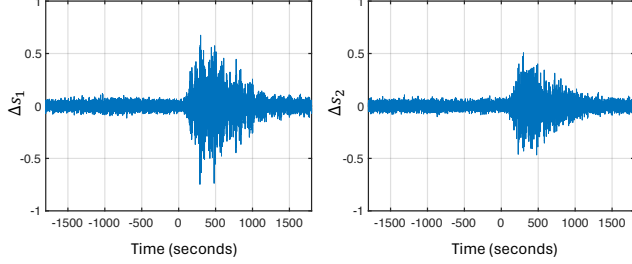


FIG. 3. Temporal traces of the two components of $\Delta\vec{s}$ orthogonal to \vec{s}_0 relative to a M7.3 earthquake occurred in Oaxaca on 23 June 2020, UTC time 15:29:05. The traces are filtered in the band 0.1 to 1.5 Hz. The origin of the temporal axis is set to the time of the earthquake.

of $\Delta\vec{s}$ orthogonal to \vec{s}_0 , namely Δs_1 and Δs_2 , extracted from the receiver of channel 1 during the Oaxaca earthquake, filtered in the band 0.1 to 1.5 Hz.

Figure 4 displays the sum of the spectrograms of the two components of the Stokes vector orthogonal to the input polarization \vec{s}_0 for channel 2, which we remind is spaced 76.5 GHz from channel 1. The spectrogram closely resembles that of Fig. 1. Figure 5 shows the temporal traces of the two components extracted from the same channel. A remarkable similarity between the traces of the two components of the Stokes vector extracted from channel 1 and channel 2 emerges from the comparison between Fig. 3 and Fig. 5. The two traces nearly overlap when the trace of channel 2 is delayed by 552.35 s. The time misalignment between the two channels can be attributed to the clock of channel 2 being out of synchronization and experiencing a slow drift, leading to lags that could accumulate to several minutes from the UTC time (for further details, refer to the supplementary material of Ref. 3).

It is valuable at this point to develop a quantitative framework for estimating the correlations between the two wavelength division multiplexing channels. Let us consider two frequencies, ω_1 and $\omega_2 = \omega_1 + \Delta\omega$ corresponding to the center frequencies of the two wavelength division multiplexing channels. We have shown in the previous analysis that the process of correlating the polarization fluctuations to the spectrum of the perturbations involves a rotation of the Poincaré sphere. This rotation aligns, for each channel, the average Stokes vector with a fixed point of the Poincaré sphere, which

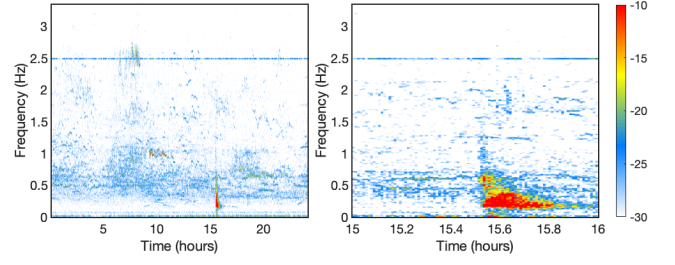


FIG. 4. Same of Fig. 1 on a channel separated by 76.5 GHz (Channel 1 is centered at 193.5805 THz and channel 2 at 193.6570 THz).

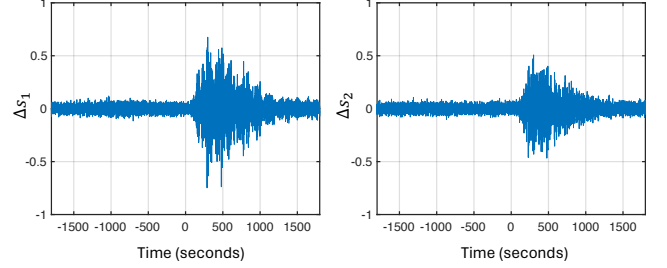


FIG. 5. Same of Fig. 3 for the same channel of Fig. 4.

we have arbitrarily chosen as the north pole. Subsequently, we analyze the deviations of the Stokes vector from this average. We have already pointed out that, apart from an immaterial time-independent rotation, this is equivalent to the use of the fluctuations of the Stokes vectors in a frame rotating with the static birefringence. Since the birefringence is frequency-dependent, the rotating frame of the two channels is different. In a frame rotating with the static birefringence at the generic frequency ω and within a first order approximation, the fluctuations of the Stokes vector at frequency ω are

$$\Delta\vec{s}'_{\omega}(z, t) = \xi \int_0^z dz' \varepsilon(z', t) \mathbf{R}_{\omega}^{-1}(z') \vec{\beta}(z') \times \vec{s}_0, \quad (121)$$

where we used Eqs. (68), (66) and (36), and we neglect, as customarily done in the theory of polarization mode dispersion, the (weak) dependence on frequency of the birefringence, but not the effect of the frequency dependence on the rotation operators. The correlation function of the fluctuations of the rotated Stokes vector at the two frequencies is

$$\langle \Delta\vec{s}'_{\omega_2}(z, t) \cdot \Delta\vec{s}'_{\omega_1}(z, t) \rangle = \xi^2 \int_0^z dz' \int_0^z dz'' \varepsilon(z', t) \varepsilon(z'', t) \left\langle \left[\mathbf{R}_{\omega_2}^{-1}(z') \vec{\beta}(z') \times \vec{s}_0 \right] \cdot \left[\mathbf{R}_{\omega_1}^{-1}(z'') \vec{\beta}(z'') \times \vec{s}_0 \right] \right\rangle. \quad (122)$$

The result of the average is (see appendix B for the detailed derivation)

$$\langle \Delta\vec{s}'_{\omega_2}(z, t') \cdot \Delta\vec{s}'_{\omega_1}(z, t) \rangle = \frac{\pi}{4} \left(\frac{2\pi c}{\lambda} \right)^2 \kappa^2 \int_0^z dz' \varepsilon(z', t') \varepsilon(z', t) F(z'), \quad (123)$$

where

$$F(z) = \exp\left(-\frac{\pi\Delta\omega^2\kappa^2 z}{8}\right). \quad (124)$$

Expressing $F(z) = \exp(-z/\Delta Z)$ with $\Delta Z = 2/(\pi^3\Delta f^2\kappa^2)$, and using the values of the systems of ref. 1, $\kappa = 0.03 \text{ ps}/\sqrt{\text{km}}$ and $\Delta f = 76.5 \text{ GHz}$, we obtain $\Delta Z \simeq 12,247 \text{ km}$. In the presence of a localized perturbation centered at $z = z_p$ over a spatial extension $\Delta z \ll \Delta Z$, we may replace $F(z')$ with $F(z_p)$ in the integral at right-hand side of Eq. (123), obtaining

$$\begin{aligned} \langle \Delta \vec{s}_{\omega_2}(z, t') \cdot \Delta \vec{s}_{\omega_1}(z, t) \rangle &\simeq \\ \frac{\pi}{4} \left(\frac{2\pi c}{\lambda} \right)^2 \xi^2 \kappa^2 F(z_p) \int_0^z dz' \varepsilon(z', t') \varepsilon(z', t), \end{aligned} \quad (125)$$

that is

$$\langle \Delta \vec{s}_{\omega_2}(z, t') \cdot \Delta \vec{s}_{\omega_1}(z, t) \rangle \simeq \langle \Delta \vec{s}_{\omega}(z, t') \cdot \Delta \vec{s}_{\omega}(z, t) \rangle F(z_p), \quad (126)$$

where at right-hand side ω is either ω_1 or ω_2 . Since the fluctuations of the Stokes vector $\Delta \vec{s}$ are isotropic on the tangent plane of the Poincaré sphere centered on the tip of \vec{s}_0 , the above equations in terms of the components on a canonical basis of the rotated Stokes space \vec{e}_i become

$$\begin{aligned} &\langle [\Delta \vec{s}_{\omega_2}(z, t') \cdot \vec{e}_i] [\Delta \vec{s}_{\omega_1}(z, t) \cdot \vec{e}_j] \rangle \\ &= \frac{1}{2} \langle \Delta \vec{s}_{\omega_2}(z, t') \cdot \Delta \vec{s}_{\omega_1}(z, t) \rangle \delta_{i,j}, \quad i, j = 1, 2, \end{aligned} \quad (127)$$

and

$$\begin{aligned} &\langle [\Delta \vec{s}_{\omega}(z, t') \cdot \vec{e}_i] [\Delta \vec{s}_{\omega}(z, t) \cdot \vec{e}_j] \rangle \\ &= \frac{1}{2} \langle \Delta \vec{s}_{\omega}(z, t') \cdot \Delta \vec{s}_{\omega}(z, t) \rangle \delta_{i,j}, \quad i, j = 1, 2, \end{aligned} \quad (128)$$

with the fluctuations of the third components zero to first order.

When a single localized perturbation is dominant over the others, the cross-correlation is proportional to the autocorrelation of the two channels, with the scaling factor $F(z_p)$. This is the case of earthquakes strongly coupled to the fiber. When, on the other hand, there are multiple perturbations scattered at different positions along the cable, the proportionality cannot be established and cross-correlation and autocorrelations have different shapes. For a given z_p , the width of the function $F(z_p)$ is the bandwidth over which the polarization of two channels at different frequencies decorrelates, which is related (but is not equal) to the bandwidth of the principal states of polarization of the fiber section from the transmitter to the position z_p along the fiber.¹⁵ This bandwidth is directly proportional to the inverse of the polarization mode dispersion coefficient, κ , multiplied by the square root of the distance from transmitter.

When a narrowband perturbation affects all channels equally at a specific point in the fiber, it might seem somehow obvious that the perturbation is fully correlated if the perturbation is applied at the receiver, that is $z_p = z$, and that the distance for considering the decorrelation of the perturbation imprinted on the channels is the distance from the point

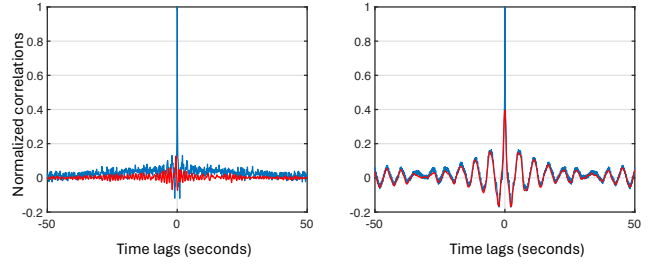


FIG. 6. Autocorrelation of Δs_1 for channel 1 (blue) with overlapped cross-correlation between channel 1 and channel 2 delayed by 552.35 s, from 0 to 12 UTC time of 23 June 2020 (left panel), and from 12 to 24 UTC time of the same day, which include the time of the earthquake (right panel).

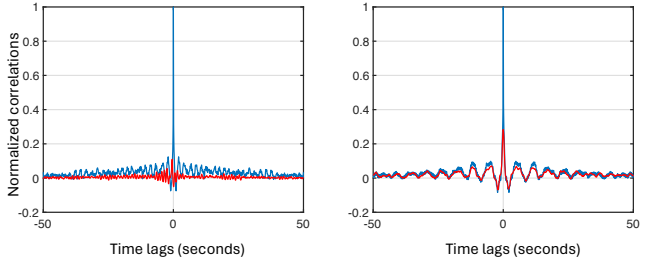


FIG. 7. Autocorrelation of Δs_2 for channel 1 (blue) with overlapped cross-correlation between channel 1 and channel 2 delayed by 552.35 s, from 0 to 12 UTC time of 23 June 2020 (left panel), and from 12 to 24 UTC time of the same day, which include the time of the earthquake (right panel). The cross-correlation is displayed with a sign inverted (see text).

where the perturbation is applied to the receiver. It may therefore appear counterintuitive the result stated by Eq. (126) that the distance affecting the depolarization is the distance of the perturbation point from the transmitter z_p . This produces the seemingly paradoxical results that a perturbation at the cable input produces a fully correlated polarization perturbation between distant channels. The explanation of this result stems from the use of a frame rotating with the static birefringence of each channel. The use of this reference frame is equivalent to the application of a backpropagation that rotates back the output polarization under the action of the static birefringence only. The output polarization of two channels does get decorrelated proportionally to the distance of the section that goes from the perturbation point to the receiver, but the backpropagation from the receiver to the transmitter compensates exactly the decorrelation that occurs in the section from the receiver to the point where the perturbation is applied, leaving uncompensated only the propagation from the point of perturbation to the transmitter.

Let us now compare the expressions that we have just derived with the data provided in ref. 1. Since the cable perturbation is inherently a nonstationary process, its correlation functions do not depend on $t - t'$ only. For a better visual representation, we decided to compare autocorrelation and cross-correlation plotting the normalized correlation of the polar-

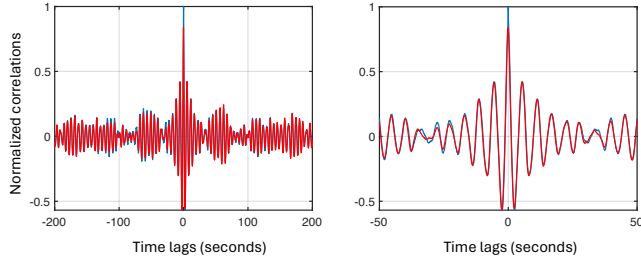


FIG. 8. Autocorrelation of Δs_1 for channel 1 (blue) with overlapped cross-correlation between channel 1 and channel 2 delayed by 552.35 s, from UTC time $t_0 - 1000$ s to $t_0 + 2000$ s where t_0 is the UTC time of the earthquake 23 June 2020 15:29:05 plotted from -200 s to 200 s (left panel), and a zoom from -50 s to 50 s (right panel).

ization traces as a function of the time difference $t - t'$, averaged over a suitable time window and normalized such that the autocorrelation for $t = t'$ is one. The time window for the average will be chosen on a case-by-case basis to highlight specific features of the process.

Figure 6 illustrates the autocorrelation of Δs_1 for channel 1 (blue), with overlapped the cross-correlation between Δs_1 extracted from channel 1 and channel 2 delayed by 552.35 s (red). The cross correlation was calculated spanning the time interval from 0 to 12 UTC time of 23 June 2020 (left panel), and the time interval, containing the time of the earthquake, from 12 to 24 UTC time of the same day (right panel). Figure 7 depicts the same curves for Δs_2 , with the cross-correlation displayed with the sign inverted. Notably, achieving consistency between the data extracted from channel 1 and channel 2 always necessitates inverting one of the components (not always the same) of the Stokes vector of one of the two channels, that we arbitrarily chose as being channel 2. A plausible explanation is that the transmission matrix, from which the output polarization of channel 2 (or channel 1) is derived, is the transpose of that pertaining to the propagation direction of channel 1 (or channel 2). The transposition of a matrix entails the inversion of the third component of the rotation vector in Stokes space, effectively resulting in an improper rotation of the Stokes space. The resulting change of the frame parity (from right-handed to left-handed) in Stokes space implies that after rotation, one of the two components of the fluctuations of the rotated Stokes vector changes its sign.

The right panels of Figs. 6 and 7 demonstrate, in agreement with our theoretical predictions, that in the presence of a dominant localized earthquake perturbation, the autocorrelation and the cross-correlation exhibit approximate proportionality, whereas they manifest different shapes when the perturbations are numerous and distributed, as in the left panels of the same figures. However, while this proportionality becomes evident for nonzero time lags, the value when the time lag equals zero appears reduced compared to the expected value. This reduction may stem from either the residual presence of distributed perturbations or a slow drift of the clock of channel 2, resulting in a misalignment of the polarization traces. This misalignment effectively produces a dilatation of the time axis of channel 2, thus reducing the narrow cross-correlation peak.

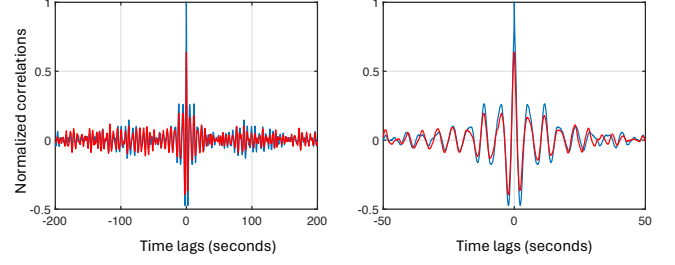


FIG. 9. Autocorrelation of Δs_2 for channel 1 (blue) with overlapped cross-correlation between channel 1 and channel 2 delayed by 552.35 s, from UTC time $t_0 - 1000$ s to $t_0 + 2000$ s where t_0 is the UTC time of the earthquake on 23 June 2020, 15:29:05 plotted from -200 s to 200 s (left panel), and a zoom from -50 s to 50 s (right panel).

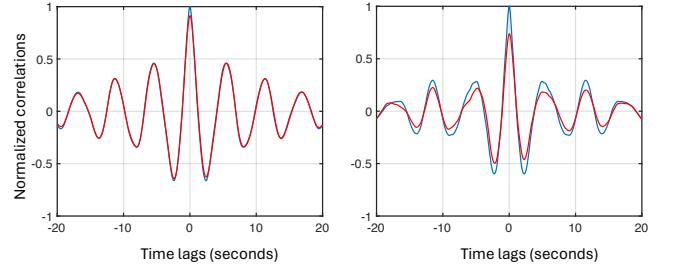


FIG. 10. In blue: autocorrelations of Δs_1 (left panel), and of Δs_2 (right panel) for channel 1. In red: cross-correlations between Δs_1 obtained from channel 1 and channel 2 (left panel) and Δs_2 obtained from channel 1 and channel 2, respectively, delayed by 552.35 s. Before processing, the signals were filtered within the frequency range of 0.1 to 1.5 Hz, corresponding to the earthquake perturbation frequency range. The time window from UTC time $t_0 - 1000$ s to $t_0 + 2000$ s where t_0 is the UTC time of the earthquake on 23 June 2020, 15:29:05.

Both of these effects become less pronounced if we narrow down the time window of the cross-correlation around the time of the earthquake. This is corroborated by the analysis of Figs. 8 and 9, where the right panels depict the same autocorrelations and cross-correlations as the right panels of Figs. 6 and 7, but calculated over a time window of 3000 s starting from 1000 s before the UTC time of the earthquake. The left panels represent the same correlations as the right panels, with enlarged windows for the time lags. The rise of the central peak is evident, along with the near overlap of the two correlation traces at non-zero time lags.

Further confirmation of the strong correlation between the polarization fluctuations of the two channels is evident when the Stokes vector deviations are filtered within the frequency range of 0.1 to 1.5 Hz, which approximately corresponds to the earthquake perturbation frequency range. This is shown in Fig. 10, which in the left panel illustrates in blue the autocorrelations of Δs_1 , while in the right panel the autocorrelations of Δs_2 , both for channel 1. Overlaid in red are the cross-correlations between Δs_1 and Δs_2 , respectively, obtained from the two channels, delayed by 552.35 s. Before processing, the signals were filtered within the frequency range of 0.1 to

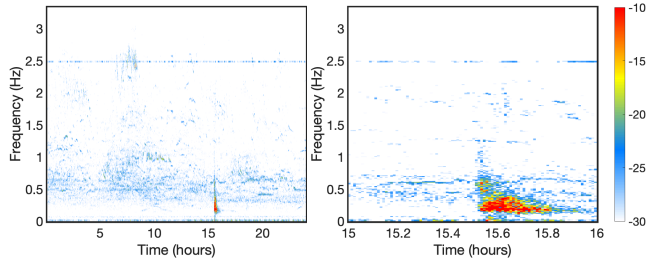


FIG. 11. Sum of the cross-spectrograms of the Δs_1 and Δs_2 of channel 1 and channel 2, relative to a M7.3 earthquake occurred in Oaxaca on 23 June 2020, UTC time 15:29:05. Left panel shows the entire day of the earthquake, the right panel a zoom of the hour of the earthquake.

1.5 Hz. For the component with more pronounced dynamics, Δs_1 , the autocorrelation and cross-correlation curves essentially coincide. For the component exhibiting smaller amplitude fluctuations (possibly because of some residual polarization dependent loss), the two curves are more distinct. This difference might be attributed to the rotation of the sphere aimed at aligning the average output Stokes vector with the north pole. The rotation could have been different for the two channels, potentially causing a slight misalignment of the cluster of polarization points due to a small rotation around the third axis of the Stokes vector.

Cross-spectrograms,¹¹ which are the time-frequency representation of the products of the short-time Fourier transforms of the polarization traces of the two channels (or equivalently, of the modulus of the short-time Fourier transform of the cross-correlations), can also provide a useful visualization of the correlations between channels. Figure 11 shows the sum of the cross-spectrograms of Δs_1 and Δs_2 of channel 1 and channel 2 for the entire day of the earthquake (left panel) and its magnification in the hour of the earthquake (right panel). The trace of channel 2 has been delayed by 552.35 s. The strong similarity with Fig. 1, representing the sum of the spectrograms of Δs_1 and Δs_2 of channel 1, is self-evident. It is also evident that the cross-spectrograms show an earthquake signature practically unaltered from the spectrograms of Fig. 1, while the background features appear more diffuse, suggesting a less localized origin. Figure 12 shows separately the cross-spectrogram of Δs_1 (left panel) and Δs_2 (right panel) of channel 1 and channel 2. Again, the cross-spectrograms displayed here show features very similar to those in Fig. 2, which presents separately the spectrograms of Δs_1 and Δs_2 of channel 1.

Let us now examine another earthquake, namely a magnitude 6.8 event with its epicenter located 200 km east of the city of Antofagasta, Chile, near the Valparaiso terminal of the Curie cable. This earthquake occurred on June 3, 2020, at UTC time 07:35:33. Figure 13 displays the sum of the spectrograms of the two components of the output Stokes vectors orthogonal to the input Stokes vector for channel 1. The left panel illustrates the entire day of the earthquake, while the right panel zooms in on a one-hour time window around the earthquake event. Compared to the Oaxaca earthquake, the

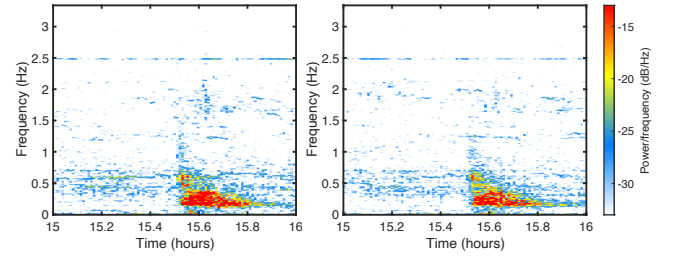


FIG. 12. Cross-spectrograms of the Δs_1 and Δs_2 of channel 1 and channel 2, relative to a M7.3 earthquake occurred in Oaxaca on 23 June 2020, UTC time 15:29:05.

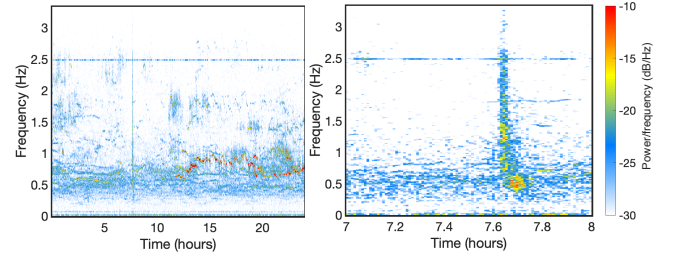


FIG. 13. Sum of the spectrograms of the two components of the $\vec{\Delta s}$ orthogonal to \vec{s}_0 relative to M6.8 earthquake occurred approximately 200 km east of the city of Antofagasta, in Chile, on 3 June 2020, UTC time 07:35:33. The abscissa reports to the UTC time. The left panel reports the entire day of the earthquake while the right panel the zoom of one hour time window around the earthquake time.

spectral signature of this event appears much weaker, suggesting a potentially lower coupling of the cable with the surrounding environment.

For this earthquake as well the database of Ref. 1 includes state of polarization data extracted from channel 1 and 2. Figure 14 displays the autocorrelation of Δs_1 of channel 1 in blue and the cross-correlation between Δs_1 of channel 1 and channel 2 in red. The left panel covers the time interval from 0 to 12 UTC time on June 3, 2020, an interval including the time of the earthquake, while the right panel covers the time interval from 12 to 24 UTC time of the same day. In both plots, Δs_1 of channel 2 was inverted. Figure 15 shows the same quantities for Δs_2 . Notice that, differently from the state of polarization data of channel 2 relative to the Oaxaca earthquake where, to make the data compatible with those of channel 1, Δs_1 was left unchanged and Δs_2 inverted, in this case Δs_1 was inverted and Δs_2 left unchanged. As we discussed previously, the change of sign of only one of the components of the Stokes vector of channel 2 is indicative of a change of parity. This could potentially result from the unitary matrix used to derive the polarization data for channel 2 being the transpose of that for channel 1, suggesting a reversal in propagation direction.

Both Figs. 14 and 15 fail to show a clear proportionality between autocorrelation and cross-correlation, because the earthquake is not the dominant source of perturbation when averaged over 12 hours. If we restrict the autocorrelations and cross-correlation to a neighbour of the earthquake, we

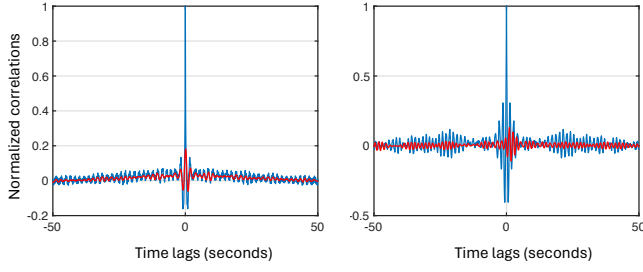


FIG. 14. Autocorrelation (blue) of Δs_1 of channel 1 and cross-correlation (red) between Δs_1 of the channel 1 and channel 2, from 0 to 12 UTC time of 3 June 2020, which include the time of the earthquake (left panel), and from 12 to 24 UTC time of the same day (right panel). The cross-correlation is displayed with a sign inverted (see text)

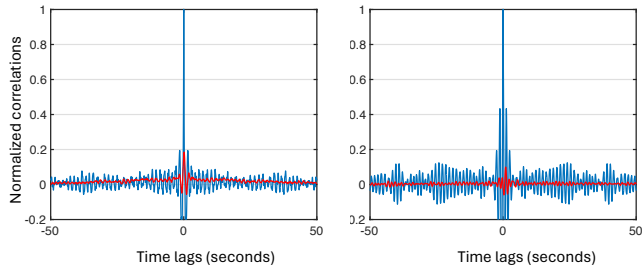


FIG. 15. Autocorrelation of Δs_2 for channel 1 (blue) with overlapped cross-correlation between channel 1 and channel 2 delayed by 519.9 s (red), from 0 to 12 UTC time of 3 June 2020, (left panel), and from 12 to 24 UTC time of the same day (right panel).

expect this proportionality to rise up. This is confirmed by looking at Figs. 16 and 17 which show the autocorrelations of Δs_1 and Δs_2 for channel 1 and the cross-correlations of the same quantities of channel 1 and 2, calculated from UTC time $t_0 - 1000$ s to $t_0 + 2000$ s where t_0 is the UTC time of the earthquake, 07:35:33 of 3 June 2020. Autocorrelations and cross-correlations have in this case a distinct similarity, as the theory suggests.

Figure 18 shows the sum of the cross-spectrograms of Δs_1 and Δs_2 of channel 1 and channel 2, on the entire day of 3 June 2020, and one hour around UTC time 07:35:33. The trace of channel 2 has been delayed by 519.9 s. Once again the similarity with the autocorrelation of 13 is self evident, although the amplitude of the cross-spectrogram appears smaller, compared with the spectrogram, when compared to the similar figures for the Oaxaca earthquake.

Let us delve deeper into the Oaxaca and Chile earthquakes through the lens of the theory established earlier in this section. Regarding the Oaxaca earthquake, the cable point closest to the epicenter of the earthquake lies approximately 2,000 km from Los Angeles. Given the loop-back configuration of the system, the transmitted signal encounters the earthquake's perturbation twice during a round-trip. Assuming the perturbation is small hence it affects the polarization linearly, we can infer that the effects of the two perturbations

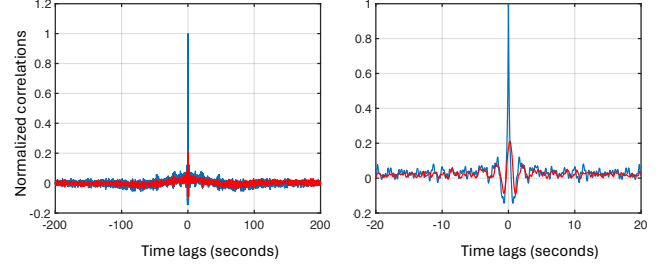


FIG. 16. Autocorrelation of Δs_1 for channel 1 (blue) with overlapped cross-correlation between channel 1 and channel 2 delayed by 519.9 s (red), from UTC time $t_0 - 1000$ s to $t_0 + 2000$ s where t_0 is the UTC time of the earthquake, 3 June 2020 07:35:33 plotted from -200 s to 200 s (left panel), and a zoom from -50 s to 50 s (right panel).

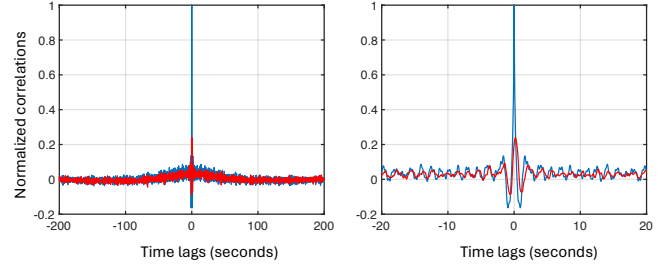


FIG. 17. Autocorrelation of Δs_2 for channel 1 (blue) with overlapped cross-correlation between channel 1 and channel 2 delayed by 519.9 s (red), from UTC time $t_0 - 1000$ s to $t_0 + 2000$ s where t_0 is the UTC time of the earthquake on 3 June 2020, 07:35:33 plotted from -200 s to 200 s (left panel), and a zoom from -50 s to 50 s (right panel).

add up. With the total length of the link from Los Angeles to Valparaiso being 10,500 km, when the signal encounters the earthquake for the first time, the propagation from the transmitter is approximately $z_p(1) \simeq 2,000$ km, resulting in $F(z_p(1)) \simeq 0.85$. When the signal encounters the earthquake

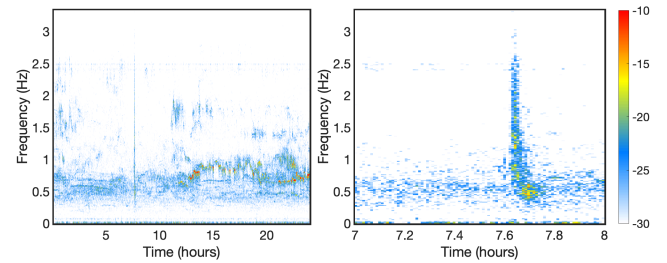


FIG. 18. Sum of the cross-spectrograms of Δs_1 and Δs_2 of channel 1 and channel 2, relative to M6.8 earthquake occurred approximately 200 km east of the city of Antofagasta, in Chile, on 3 June 2020, UTC time 07:35:33. The trace of channel 2 has been delayed by 519.9 s. The abscissa reports to the UTC time. The left panel reports the entire day of the earthquake while the right panel the zoom of one hour time window around the earthquake time.

for the second time, the distance traveled from the transmitter is $z_p(2) \simeq 21,000 - 2,000 = 19,000$ km, leading to $F(z_p(2)) \simeq 0.21$. Assuming equal efficiency of modulation in both passes, the ratio between cross-correlation and autocorrelation would be approximately $0.5 \cdot 0.85 + 0.5 \cdot 0.21 = 0.531$, yet cross-correlation and autocorrelation displayed in Figs. 8 and 9 appear nearly identical, at least for nonzero time lags where the effect of the clock misalignment is negligible. This suggests that the coupling with the earthquake is likely to be much stronger in the forward direction than in the backward. We speculate that a possible reason could be that the polarization modulation is imprinted in the fiber from Los Angeles to Valparaiso on a clean signal, whereas in the fiber from Valparaiso to Los Angeles on a signal strongly depolarized by the amplified spontaneous emission of the inline amplifiers. Notice that the cable was designed for one-way operation, and hence the loop-back arrangement makes the amplified emission noise power close to the receiver in Los Angeles approximately double the system's nominal value. Since the receiver can faithfully decode the signal modulation even in the loop-back configuration, it can also detect the additional polarization modulation imprinted by environmental perturbations on a polarized optical field near the transmitter. On the contrary, polarization modulation may be less efficient on the return fiber because it is applied on a signal considerably depolarized by the amplified emission noise power generated by nearly twice the number of amplifiers specified in the system's design.

Concerning the Chile earthquake, we can assume that the cable is perturbed around $z_p \simeq 10,000$ km for both passes, resulting in $F(z_p) \simeq 0.44$. Again, a significant, although smaller than the previous case, correlation between the two traces is expected and confirmed by the experimental traces in Figs. 16 and 17.

These observations suggest that, in principle, within a single-pass configuration of an operational transmission system, cross-correlation between two closely spaced channels, whose spacing can be optimized for maximum accuracy, may permit the localization of the position on the link where an earthquake occurs. The optimization involves the choice of a frequency spacing maximizing the sensitivity of $F(z_p)$ on a z_p ranging from 0 to the link span z . A good recipe may be setting $\Delta z \simeq z$.

To conclude the analysis, we will use the “continuous” data provided in ref. 1 to highlight the impressive sensitivity at sub-hertz frequencies of environmental sensing achieved through the detection of the light polarization. Furthermore, we will experimentally confirm that the state of polarization is primarily sensitive to variations of the hydrostatic pressure rather than to mechanical vibrations in the environment. Environmental vibrations are likely to be decoupled from the fiber due to the loose-tube configuration of the cable and the presence of petroleum jelly in which the fibers are immersed.

Figures 19 and 20 (see also refs. 3 and 4) depict the sum of the spectrograms of the two components of the Stokes vector orthogonal to the input state of polarization, recorded from June 1, 2022, to July 12, 2022 for channel 1 (Fig. 19) and from June 2, 2022, to June 30, 2022 for channel 2 (Fig. 20).

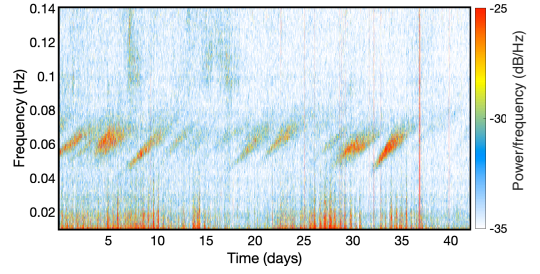


FIG. 19. Sum of the spectrograms of the two components of $\Delta \vec{s}$ orthogonal to \vec{s}_0 , acquired from channel 1, between June 1, 2022, and July 12, 2022. The abscissa represents the number of days elapsed since June 1, 2022.

Two prominent features are observable. First, there are spectral features attributed to ocean swells, which appear as dispersive wave structures. Remarkably, these structures are also clearly visible in spectrograms obtained from onshore seismographs near Los Angeles.³ Notably, these structures are exclusively present in the primary microseism band and lack a corresponding second-harmonic spectral signature in the secondary microseism band. The secondary microseism is the second-harmonic signal generated by the phase-matched excitation by pressure variations on the seafloor of two nearly counterpropagating seismic waves. The secondary microseism is clearly visible in spectrograms from on-shore seismographs (see Fig. 4, panels (B) and (C), of ref. 3) whereas it is absent in Figs. 19 and 20. This observation suggests that the state of polarization is relatively insensitive to vibrations but highly sensitive to strain induced by the direct action of pressure variations caused by ocean swells.

The second spectral feature discerned from the analysis of the spectrogram is a very distinct semidiurnal modulation at around 20 mHz. This feature arises from the modulation of the pressure applied to the fiber caused by ocean tides. It is remarkable that this impressive sensitivity to ultralow frequency perturbations was achieved through the use of a laser with a linewidth in the hundreds of kHz range, a manifestation of the immunity of the laser polarization from phase noise. Achieving comparable sensitivity at such low frequencies would be challenging, if at all possible, using phase even with lasers of ultralow linewidth.

X. CONCLUSIONS

In this paper, we initially established a theoretical framework for understanding the sensing capabilities of optical fibers. We delineated the advantages and limitations associated with utilizing polarization-averaged optical phase and the light polarization as sensing tools, showing the distinct advantage of polarization over phase to discriminate sub-hertz environmental processes. Subsequently, we proposed a scheme capable of extracting the spectrum of perturbations affecting the cable by detecting the state of polarization of the back-reflected light. Exploiting the extensive dataset of ref. 1, we

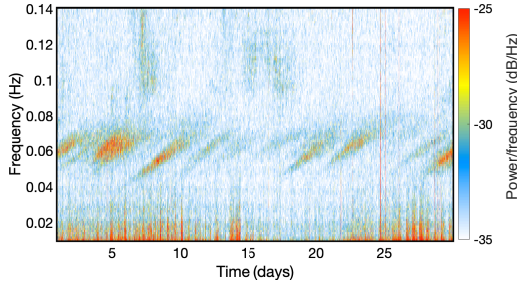


FIG. 20. Sum of the spectrograms of the two components of $\Delta \vec{s}'$ orthogonal to \vec{s}_0 , acquired from channel 2, between June 2, 2022, and June 30, 2022. The abscissa represents the number of days elapsed since June 1, 2022.

discussed two examples of earthquake detection and the detection of sea swells and ocean tides through the state of polarization reconstructed by the receiver of the Curie cable. Finally, we gave the analytical expression of the polarization cross-correlations between two channels at nearby frequencies and demonstrated how the analysis of these correlations can provide valuable insights into the localization of earthquakes.

Appendix A: Continuous limit of Eqs. (58) and (59)

In this appendix, we derive the continuous limit of Eqs. (58) and (59). After multiplying and dividing by the sampling time T , Eqs. (51) and (52) become

$$\tilde{N}(\Omega_k) = \frac{1}{nT} \sum_{h=0}^{n-1} N(hT) \exp(i\Omega_k hT) T, \quad (\text{A1})$$

$$\tilde{\varphi}(\Omega_k) = \frac{1}{nT} \sum_{h=0}^{n-1} \varphi(hT) \exp(i\Omega_k hT) T. \quad (\text{A2})$$

Letting T tend to zero and n to infinity while maintaining $nT = T_{\text{win}}$ finite, T becomes dt , hT in the exponents becomes a continuous time t and the sums transform into integrals. Thus, we arrive at the continuous limit of these expressions as

$$\tilde{N}_0(\Omega) = \frac{1}{T_{\text{win}}} \int_0^{T_{\text{win}}} \exp(i\Omega t) N_0(t) dt, \quad (\text{A3})$$

and

$$\tilde{\varphi}(\Omega) = \frac{1}{T_{\text{win}}} \int_0^{T_{\text{win}}} \exp(i\Omega t) \varphi(t) dt. \quad (\text{A4})$$

Strictly speaking, Eq. (53) dictates that Ω takes on the discrete values $\Omega = 2\pi k/(nT) = 2\pi k/T_{\text{win}}$, with $k \in \mathbb{Z}$. We removed the dependence on the integer k because we assume that Ω is analytically continued over the entire real axis. Again, like $1/n$ in the discrete case, the normalization factor $1/T_{\text{win}}$ ensures that the peak amplitude of the Fourier transform of a sinusoidal modulation is independent of the time window T_{win} .

In the continuous limit, the laser phase noise is negligible over the signal if

$$|\tilde{N}_0(\Omega)|^2 \ll |\Omega|^2 |\tilde{\varphi}(\Omega)|^2. \quad (\text{A5})$$

Inserting into $|\tilde{N}_0(\Omega)|^2$ the expression (A3), averaging the result and using Eq. (47) produces the equality

$$\langle |\tilde{N}_0(\Omega)|^2 \rangle = \frac{2\pi\nu}{T_{\text{win}}}. \quad (\text{A6})$$

Inserting this expression into Eq. (A5) and using the definition $f = \Omega/(2\pi)$ yields

$$\nu \ll 2\pi |f|^2 |\tilde{\varphi}(2\pi f)|^2 T_{\text{win}}, \quad (\text{A7})$$

which is the continuous limit of Eq. (58). Using now the definition $f = 1/T_f$, we obtain the continuous limit of Eq. (59), namely

$$\nu \ll 2\pi |f| |\tilde{\varphi}(2\pi f)|^2 \frac{T_{\text{win}}}{T_f}. \quad (\text{A8})$$

Appendix B: Derivation of Eq. (123)

In this appendix, we detail the derivation of Eq. (123). Equation (122) can be rewritten as

$$\langle \Delta \vec{s}'_{\omega_2}(z, t) \Delta \vec{s}'_{\omega_1}(z, t) \rangle = \xi^2 \int_0^z dz' \int_0^z dz'' \varepsilon(z', t) \varepsilon(z'', t) A(z', z''). \quad (\text{B1})$$

where

$$A(z', z'') = \left\langle \left[\mathbf{R}_{\omega_2}^{-1}(z') \vec{\beta}(z') \times \vec{s}_0 \right] \cdot \left[\mathbf{R}_{\omega_1}^{-1}(z'') \vec{\beta}(z'') \times \vec{s}_0 \right] \right\rangle. \quad (\text{B2})$$

If we define the auxiliary process $\vec{\beta}_0(z) = \mathbf{R}_{\omega_1}^{-1}(z) \vec{\beta}(z)$, Eq. (B2) becomes

$$A(z', z'') = \left\langle \left[\mathbf{R}_{\Delta\omega}^{-1}(z') \vec{\beta}_0(z') \times \vec{s}_0 \right] \cdot \left[\vec{\beta}_0(z'') \times \vec{s}_0 \right] \right\rangle, \quad (\text{B3})$$

with

$$\mathbf{R}_{\Delta\omega}^{-1}(z) = \mathbf{R}_{\omega_2}^{-1}(z) \mathbf{R}_{\omega_1}(z). \quad (\text{B4})$$

Expanding the scalar product inside the integral yields

$$A(z', z'') = A_1(z', z'') - A_2(z', z''), \quad (\text{B5})$$

where

$$A_1(z', z'') = \left\langle \mathbf{R}_{\Delta\omega}^{-1}(z') \vec{\beta}_0(z') \cdot \vec{\beta}_0(z'') \right\rangle, \quad (\text{B6})$$

and

$$A_2(z', z'') = \left\langle \left[\mathbf{R}_{\Delta\omega}^{-1}(z') \vec{\beta}_0(z') \cdot \vec{s}_0 \right] \left[\vec{\beta}_0(z'') \cdot \vec{s}_0 \right] \right\rangle. \quad (\text{B7})$$

If we assume the delta function approximation for the correlation function of the birefringence, Eq. (71), the same expression applies to $\vec{\beta}_0(z)$ because an isotropic rotation does not change the statistics of the isotropic vector $\vec{\beta}(z)$

$$\langle \vec{\beta}_0(z') \cdot \vec{\beta}_0(z'') \rangle = 2L_f \langle \beta^2 \rangle \delta(z' - z''). \quad (\text{B8})$$

The delta function correlation permits the consideration of the case $z' = z''$ only. As customarily done in the theory of polarization mode dispersion, we include the dependence of the birefringence on frequency only in the rotation operators. If we set $\vec{\beta} = \vec{\beta}(\omega_1)$ as the birefringence at $\omega = \omega_1$, the rotation vector Eq. (B4) has the form

$$\mathbf{R}_{\Delta\omega}^{-1}(z) = \prod_{z'=z}^{z'=0} \exp \left[-dz \vec{\beta}(\omega_2)(z') \times \right] \prod_{z'=0}^{z'=z} \exp \left[dz \vec{\beta}(\omega_1)(z') \times \right], \quad (\text{B9})$$

where the products are ordered from right to left. Assume now the following dependence of the birefringence on frequency

$$\vec{\beta}(\omega_2) = \vec{\beta}(\omega_1) + \frac{\vec{\beta}(\omega_1)}{\omega_0}(\omega_2 - \omega_1), \quad (\text{B10})$$

which implies parallelism between $\vec{\beta}(\omega_2)$ and $\vec{\beta}(\omega_1)$. Separating the inner term in the products in Eq. (B9) we obtain

$$\begin{aligned} \mathbf{R}_{\Delta\omega}^{-1}(z) &= \prod_{z'=z-dz}^{z'=0} \exp \left[-dz \vec{\beta}(\omega_2)(z') \times \right] \\ &\quad \exp \left[-dz \vec{\beta}(\omega_2)(z) \times \right] \exp \left[dz \vec{\beta}(\omega_1)(z) \times \right] \\ &\quad \prod_{z'=0}^{z'=z-dz} \exp \left[dz \vec{\beta}(\omega_1)(z') \times \right], \end{aligned} \quad (\text{B11})$$

which using the fact that $\vec{\beta}(\omega_1)(0)$ and $\vec{\beta}(\omega_2)(0)$ are parallel, becomes

$$\begin{aligned} \mathbf{R}_{\Delta\omega}^{-1}(z) &= \prod_{z'=z-dz}^{z'=0} \exp \left[-dz \vec{\beta}(\omega_2)(z') \times \right] \\ &\quad \exp \left\{ -dz \left[\vec{\beta}(\omega_2)(z) - \vec{\beta}(\omega_1)(z) \right] \times \right\} \\ &\quad \prod_{z'=0}^{z'=z-dz} \exp \left[dz \vec{\beta}(\omega_1)(z') \times \right], \end{aligned} \quad (\text{B12})$$

and using Eq. (B10)

$$\begin{aligned} \mathbf{R}_{\Delta\omega}^{-1}(z) &= \prod_{z'=z-dz}^{z'=0} \exp \left[-dz \vec{\beta}(\omega_2)(z') \times \right] \\ &\quad \exp \left[-dz \frac{\vec{\beta}(\omega_1)}{\omega_0}(\omega_2 - \omega_1) \times \right] \\ &\quad \prod_{z'=0}^{z'=z-dz} \exp \left[dz \vec{\beta}(\omega_1)(z') \times \right], \end{aligned} \quad (\text{B13})$$

For the independence of the rotations, we can average the inner term separately from the others. Using now the property of Gaussian operators

$$\langle \exp(\mathbf{G}) \rangle = \exp \left(\frac{1}{2} \langle \mathbf{G}^2 \rangle \right), \quad (\text{B14})$$

and the property that holds for any isotropic vector $\vec{\beta}(z')$

$$\left\langle \left\{ dz \left[\vec{\beta}(z')/\omega_0 \right] \times \right\}^2 \right\rangle = -\frac{2}{3} \frac{\langle |\vec{\beta}(z')|^2 \Delta\omega^2 \rangle dz^2}{\omega_0^2} \mathbb{1}, \quad (\text{B15})$$

and the equality

$$\left\langle |\vec{\beta}(z')|^2 \right\rangle dz^2 = 2L_f \langle \beta^2 \rangle dz, \quad (\text{B16})$$

which is the limit for $z'' \rightarrow z'$ of Eq. (71), we obtain after averaging the inner term

$$\begin{aligned} \mathbf{R}_{\Delta\omega}^{-1}(z) &= \exp \left(-\frac{2L_f \langle \beta^2 \rangle \Delta\omega^2 dz}{3\omega_0^2} \right) \mathbb{1} \\ &\quad \prod_{z'=z-dz}^{z'=0} \exp \left[-dz \vec{\beta}(\omega_2)(z') \times \right] \\ &\quad \prod_{z'=0}^{z'=z-dz} \exp \left[dz \vec{\beta}(\omega_1)(z') \times \right], \end{aligned} \quad (\text{B17})$$

Iterating the procedure, we obtain

$$\langle \mathbf{R}_{\Delta\omega}^{-1}(z) \rangle = \exp \left(-\frac{2L_f \langle \beta^2 \rangle \Delta\omega^2 z}{3\omega_0^2} \right) \mathbb{1}. \quad (\text{B18})$$

In Eq. (B6) $\vec{\beta}_0(z)$ differs from $\vec{\beta}(z)$ for a constant rotation. Since this equation is nonzero only for $z' = z''$ and applying a constant rotation to the two terms of a scalar product does not affect the result, we may replace $\vec{\beta}_0(z')$ with $\vec{\beta}(z')$. Noting now that $\mathbf{R}_{\Delta\omega}^{-1}(z')$ contains the birefringence of the fiber segments before the section z' we may perform the average of the rotation independently of $\vec{\beta}(z')$ obtaining

$$A_1(z', z'') = 2L_f \langle \beta^2 \rangle \exp \left(-\frac{2L_f \langle \beta^2 \rangle \Delta\omega^2 z'}{3\omega_0^2} \right) \delta(z' - z''). \quad (\text{B19})$$

In Eq. (B7) we notice that $\vec{\beta}_0(z)$ preserves the isotropy of $\vec{\beta}(z)$, and that the absolute orientation of isotropic vectors is immaterial. Again for the property that $A_1(z', z'')$ is nonzero only for $z' = z''$, $\vec{\beta}_0(z')$ and $\vec{\beta}(z')$ differ only for a constant rotation, and hence we can replace $\vec{\beta}_0(z')$ with $\vec{\beta}(z')$. With the same arguments used to derive Eq. (B19), we can also in this case average the rotation operator independently of $\vec{\beta}(z')$ obtaining

$$A_2(z', z'') = \frac{1}{3} 2L_f \langle \beta^2 \rangle \exp \left(-\frac{2L_f \langle \beta^2 \rangle \Delta\omega^2 z'}{3\omega_0^2} \right) \delta(z' - z''). \quad (\text{B20})$$

where we used that $\left\langle \left[\vec{\beta}_0(z') \cdot \vec{s}_0 \right] \left[\vec{\beta}_0(z') \cdot \vec{s}_0 \right] \right\rangle = \langle \vec{\beta}_0(z')^2 \rangle / 3$ for the isotropy of $\vec{\beta}_0(z')$. Adding the two contributions we obtain

$$A(z', z'') = \frac{2}{3} 2L_f \langle \beta^2 \rangle \exp \left(-\frac{2L_f \langle \beta^2 \rangle \Delta\omega^2 z}{3\omega_0^2} \right) \delta(z' - z''). \quad (\text{B21})$$

Using Eq. (75) we obtain

$$A(z', z'') = \frac{\pi}{4} \omega_0^2 \kappa^2 \exp \left(-\frac{\pi \kappa^2 \Delta\omega^2 z}{8} \right) \delta(z' - z''). \quad (\text{B22})$$

Entering this result into Eq. (B1) we obtain Eq. (123).

- ¹Z. Zhan, “Curie Data - Zhan et al. (2021),” (2020), <https://data.caltech.edu/records/50509-xhf30>.
- ²G. Marra, C. Clivati, R. Luckett, A. Tampellini, J. Kronjäger, L. Wright, A. Mura, F. Levi, S. Robinson, A. Xuereb, B. Baptie, and D. Calonico, “Ultrastable laser interferometry for earthquake detection with terrestrial and submarine cables,” *Science* **361**, 486–490 (2018), <https://www.science.org/doi/pdf/10.1126/science.aat4458>.
- ³Z. Zhan, M. Cantono, V. Kamalov, A. Mecozzi, R. Müller, S. Yin, and J. C. Castellanos, “Optical polarization-based seismic and water wave sensing on transoceanic cables,” *Science* **371**, 931–936 (2021), <https://www.science.org/doi/pdf/10.1126/science.abe6648>.
- ⁴A. Mecozzi, M. Cantono, J. C. Castellanos, V. Kamalov, R. Muller, and Z. Zhan, “Polarization sensing using submarine optical cables,” *Optica* **8**, 788–795 (2021), <https://opg.optica.org/optica/abstract.cfm?URI=optica-8-6-788>.
- ⁵N. J. Lindsey, T. C. Dawe, and J. B. Ajo-Franklin, “Illuminating seafloor faults and ocean dynamics with dark fiber distributed acoustic sensing,” *Science* **366**, 1103–1107 (2019), <https://www.science.org/doi/pdf/10.1126/science.aay5881>.
- ⁶M. Landrø, L. Bouffaut, H. J. Kriesell, J. R. Potter, R. A. Rørstadbotnen, K. Taweesintananon, S. E. Johansen, J. K. Brenne, A. Haukanes, O. Schjelderup, and F. Storvik, “Sensing whales, storms, ships and earthquakes using an arctic fibre optic cable,” *Scientific Reports* **12**, 19226 (2022), <https://doi.org/10.1038/s41598-022-23606-x>.
- ⁷K. S. Y. Skarvang, S. Bjørnstad, R. A. Rørstadbotnen, K. Bozorgebrahimi, and D. R. Hjelme, “Observation of local small magnitude earthquakes using state of polarization monitoring in a 250km passive arctic submarine communication cable,” in *Optical Fiber Communication Conference (OFC) 2023* (Optica Publishing Group, 2023) p. W1J.2.
- ⁸This property is an immediate consequence of the isomorphism between $SU(2)$ and $SO(3)$ (the group of three dimensional rotations around the origin of Stokes space) and of the fact that the concatenation of rotations is still a rotation.
- ⁹J. P. Gordon and H. Kogelnik, “PMD fundamentals: Polarization mode dispersion in optical fibers,” *Proceedings of the National Academy of Sciences* **97**, 4541–4550 (2000), <https://www.pnas.org/content/97/9/4541.full.pdf>.
- ¹⁰J. Sakurai and J. Napolitano, *Modern Quantum Mechanics* (Cambridge University Press, 2017).
- ¹¹A. V. Oppenheim, R. W. Schaffer, and J. R. Buck, *Discrete-Time Signal Processing*, 2nd ed., Pearson education signal processing series (Upper Saddle River, N.J.: Prentice Hall, 1999).
- ¹²J. P. Gordon, “Statistical properties of polarization mode dispersion,” in *Polarization Mode Dispersion* (Springer New York, New York, NY, 2005) pp. 52–59.
- ¹³A. Galtarossa, L. Palmieri, M. Schiano, and T. Tambosso, “Measurement of birefringence correlation length in long, single-mode fibers,” *Opt. Lett.* **26**, 962–964 (2001).
- ¹⁴J. Wuttke, P. Krummrich, and J. Rosch, “Polarization oscillations in aerial fiber caused by wind and power-line current,” *IEEE Photonics Technology Letters* **15**, 882–884 (2003).
- ¹⁵M. Shttaif and A. Mecozzi, “Study of the frequency autocorrelation of the differential group delay in fibers with polarization mode dispersion,” *Opt. Lett.* **25**, 707–709 (2000).
- ¹⁶S. Donadello, C. Clivati, A. Govoni, L. Margheriti, M. Vassallo, D. Brenda, M. Hovsepyan, E. K. Bertacco, R. Concas, F. Levi, A. Mura, A. Herrero, F. Carpentieri, and D. Calonico, “Seismic monitoring using the telecom fiber network,” *Communications Earth & Environment* **5**, 178 (2024).
- ¹⁷A. Mecozzi, C. Antonelli, M. Mazur, N. Fontaine, H. Chen, L. Dallachiesa, and R. Ryf, “Use of optical coherent detection for environmental sensing,” *J. Lightwave Technol.* **41**, 3350–3357 (2023).
- ¹⁸M. Mazur, J. C. Castellanos, R. Ryf, E. Börjeson, T. Chodkiewicz, V. Kamalov, S. Yin, N. K. Fontaine, H. Chen, L. Dallachiesa, S. Corteselli, P. Copping, J. Gripp, A. Mortelette, B. Kowalski, R. Dellinger, D. T. Neilson, and P. Larsson-Edefors, “Transoceanic phase and polarization fiber sensing using real-time coherent transceiver,” in *Optical Fiber Communication Conference (OFC) 2022* (Optica Publishing Group, 2022) p. M2F.2, <https://opg.optica.org/abstract.cfm?URI=OFC-2022-M2F.2>.
- ¹⁹M. Mazur, N. K. Fontaine, M. Kelleher, V. Kamalov, R. Ryf, L. Dallachiesa, H. Chen, D. T. Neilson, and F. Quinlan, “Advanced distributed submarine cable monitoring and environmental sensing using constant power probe signals and coherent detection,” (2023), arXiv:2303.06528 [eess.SP].
- ²⁰F. Yaman, Y. Li, S. Han, T. Inoue, E. Mateo, and Y. Inada, “Polarization sensing using polarization rotation matrix eigenvalue method,” in *Optical Fiber Communication Conference (OFC) 2023* (Optica Publishing Group, 2023) p. W1J.7.
- ²¹L. Costa, S. Varughese, P. Mertz, V. Kamalov, and Z. Zhan, “Localization of seismic waves with submarine fiber optics using polarization-only measurements,” *Communications Engineering* **2**, 86 (2023).
- ²²A. Galtarossa, D. Grosso, L. Palmieri, and L. Schenato, “Reflectometric characterization of hinges in optical fiber links,” *IEEE Photonics Technology Letters* **20**, 854–856 (2008).